# Magnetic field induced topological semimetals near the quantum critical point of pyrochlore iridates

Taekoo Oh,[1,2,3] Hiroaki Ishizuka,[4] and Bohm-Jung Yang[1,2,3,*]

[1]*Department of Physics and Astronomy, Seoul National University, Seoul 08826, Korea*
[2]*Center for Correlated Electron Systems, Institute for Basic Science (IBS), Seoul 08826, Korea*
[3]*Center for Theoretical Physics (CTP), Seoul National University, Seoul 08826, Korea*
[4]*Department of Applied Physics, University of Tokyo, Hongo, Bunkyo-ku, Tokyo 113-8656, Japan*

(Received 5 July 2018; revised manuscript received 30 July 2018; published 8 October 2018)

Motivated by the recent experimental observation of anomalous magnetotransport properties near the Mott quantum critical point (QCP) of pyrochlore iridates, we study the generic topological band structure near QCP in the presence of magnetic field. We have found that the competition between different energy scales can generate various topological semimetal phases near QCP. Here the central role is played by the presence of a quadratic band crossing (QBC) with fourfold degeneracy in the paramagnetic band structure. Due to the large band degeneracy and strong spin-orbit coupling, the degenerate states at QBC can show an anisotropic Zeeman effect as well as the conventional isotropic Zeeman effect. Through the competition between three different magnetic energy scales including the exchange energy between Ir electrons and two Zeeman energies, various topological semimetals can be generated near QCP. Moreover, we have shown that these three magnetic energy scales can be controlled by modulating the magnetic multipole moment (MMM) of the cluster of spins in a unit cell, which can couple to the intrinsic MMM of the degenerate states at QBC. We propose the general topological band structure under magnetic field achievable near QCP, which would facilitate the experimental discovery of novel topological semimetal states in pyrochlore iridates.

DOI: 10.1103/PhysRevB.98.144409

## I. INTRODUCTION

Electron correlation and spin-orbit coupling are two quintessential ingredients underlying vast emergent physical phenomena in condensed matter [1,2]. In particular, when these two energy scales are comparable to the electron bandwidth, various correlated phases with novel topological properties are expected to appear in general [3–7]. Pyrochlore iridates with the chemical formula $R_2Ir_2O_7$ [$R$: a rare-earth ion; see Fig. 1(a)] are a representative example of such correlated topological systems that can potentially host various intriguing electronic states [1,2]. In the paramagnetic metal (PM) phase, it was theoretically predicted that these materials have a quadratic band crossing (QBC) with doubly degenerate hole-like and electron-like bands touching at the Γ point [8]. A recent ARPES study on $Pr_2Ir_2O_7$ [9] finds electron dispersion which conforms closely to this prediction. When a magnetic transition occurs below the temperature $T_N$, a variety of interesting electronic states possibly show up from the QBC. For instance, an antiferromagnetic (AF) Weyl semimetal (WSM) phase is theoretically predicted to exist between a PM and an AF insulator (AFI) with all-in all-out (AIAO) type magnetic ordering as shown in Figs. 1(b) and 1(c) [3,8,10–12].

On the other hand, in reality, except for the case of $R$ = Pr where the PM phase persists down to the lowest temperature accessible, the WSM state only appears in a small window at the boundary between PM and AFI phases (Fig. 2). However, by substituting $R$ sites by the ions with larger radius or applying hydrostatic pressure, one can reduce $T_N$ systematically and approach the quantum critical point (QCP), around which a semimetallic ground state with AF ordering may be achievable [13]. Interestingly, in systems close to the QCP such as those with $R$ = Nd or Pr, anomalous transport properties are observed such as anomalous Hall effects, metallic states at AIAO domain walls, and magnetic field induced metal-insulator transitions [14–22]. In particular, a recent study of $(Nd_{1-x}Pr_x)_2Ir_2O_7$ under pressure in which $T_N$ has been systematically tuned to reach the QCP has demonstrated unusual magnetotransport properties near the QCP, which might be associated with topological semimetal phases emerging near the QCP under magnetic field [13]. The accumulated experimental and theoretical results from preceding studies are summarized in the schematic phase diagram shown in Fig. 2, implying that applying magnetic field to the system located near the QCP is a promising way to achieve various topological semimetals with point or line nodes.

The main purpose of the present theoretical study is to provide a general theoretical framework to understand the magnetic field induced topological semimetals emerging near the QCP of pyrochlore iridates. To address this issue, we start from the PM phase with QBC and approach the QCP by introducing AIAO ordering together with magnetic field. The QBC at the Γ point can be described by the states carrying the total angular momentum $J = 3/2$. Due to the large total angular momentum $J$ and strong spin-orbit coupling, the Zeeman coupling shows a nontrivial feature: the Zeeman

*bjyang@snu.ac.kr

 ©2018 American Physical Society

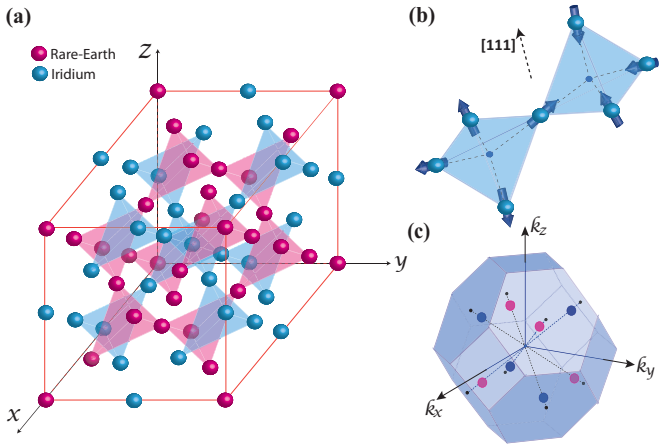


FIG. 1. (a) The lattice structure of pyrochlore iridates. (b) All-in all-out (AIAO) magnetic ordering. (c) Distribution of Weyl points in the Weyl semimetal related with AIAO ordering.

field $\vec{H}$ can give rise to an unconventional anisotropic Zeeman effect ($\propto \vec{H} \cdot \vec{J}^3$) as well as the usual isotropic Zeeman coupling ($\propto \vec{H} \cdot \vec{J}$). Moreover, an additional magnetic energy scale associated with the AIAO ordering exists. Since the exchange energy associated with AIAO ordering and the two different Zeeman energies are comparable near the QCP, the competition between them can bring about various novel topological semimetal phases according to the low-energy theory. In terms of microscopic lattice degrees of freedom, we show that the interplay between three different magnetic energy scales can be compactly described in terms of magnetic multipole moments (MMMs) of the cluster of four spins in a tetrahedron. Magnetic field induced modulation of MMMs of the unit cell and its coupling to the intrinsic MMMs of the degenerate states at QBC lie at the heart of emergent

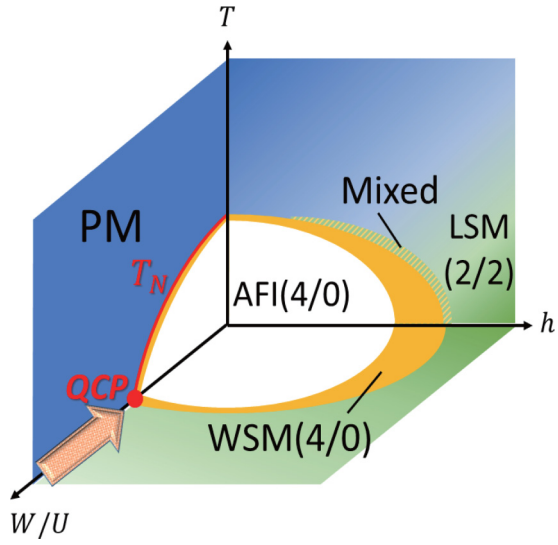


FIG. 2. Schematic phase diagram near the quantum critical point (QCP) in the space of Coulomb interaction $U$, temperature $T$, and magnetic field $h$ for given electron bandwidth. PM is a paramagnetic metal, AFI(4/0) is an antiferromagnetic insulator with AIAO, WSM(4/0) is a Weyl semimetal with AIAO, and LSM(2/2) is a line-node semimetal with 2-in 2-out ordering.

topological semimetals near the QCP of pyrochlore iridates under magnetic field.

The paper is organized as follows. In Sec. II, we first introduce the effective theory at the Γ point, and describe topological semimetals induced by AIAO ordering. Magnetic field induced topological semimetals are described by considering the Zeeman field as well as AIAO ordering in Sec. III. In Sec. IV, we study the lattice model, and explain its relation to effective Hamiltonian analysis in terms of cluster magnetic multipole moments (CMMMs). Finally, in Sec. V, we conclude.

## II. QUADRATIC BAND CROSSING AND AIAO ORDERING

The QBC of the PM state [8,9,12,23] is shown in Fig. 3(a). Since each eigenstate is doubly degenerate due to the time-reversal and inversion symmetries, the QBC at Γ has fourfold degeneracy with the total angular momentum $J = 3/2$. The low-energy physics near the QBC can be described by the so-called Luttinger Hamiltonian [24] given by

$$\mathcal{H}_0(\vec{k}) = \epsilon_0(\vec{k}) + \sum_{i=1}^{5} d_i(\vec{k})\Gamma_i, \tag{1}$$

where $\epsilon_0(\vec{k}) = k^2/2m$ and $\Gamma_i$ is a $4 \times 4$ gamma matrix satisfying the Clifford algebra $\{\Gamma_i, \Gamma_j\} = 2\delta_{ij}$ $(i, j = 1 \sim 5)$. By defining ten additional Hermitian matrices as $\Gamma_{ij} = [\Gamma_i, \Gamma_j]/2i$ and the identity matrix, one can find a complete set of sixteen Hermitian $4 \times 4$ matrices. The detailed form of the function $d_{1\sim5}(\vec{k})$ constrained by the cubic symmetry at Γ is shown in Appendix A.

When Ir AIAO ordering is developed below $T_N$, the QBC at Γ splits into four pairs of Weyl points (WPs) in which each pair is aligned along either [111] or its three other symmetry-related directions [12]. Such an emerging WSM with eight WPs can be described by adding $\mathcal{H}_{\mathrm{AIAO}} = -\alpha\Gamma_{45}$ with $\alpha \propto U m_{\mathrm{AIAO}}$ to Eq. (1) where $U$ is the local Coulomb repulsion and $m_{\mathrm{AIAO}}$ represents the local magnetic moment of the AIAO state. Since the separation between the WP pair on the [111]

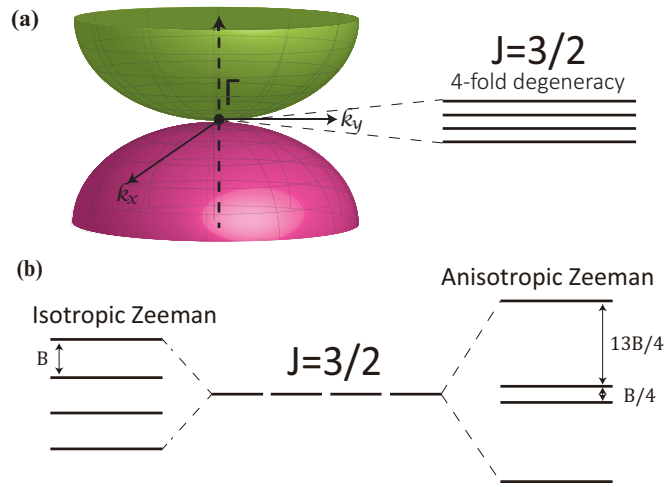


FIG. 3. (a) The band structure near the quadratic band crossing (QBC). (b) The energy level splitting of $J = 3/2$ states at the Γ point due to isotropic and anisotropic Zeeman terms, respectively.

axis is proportional to $\sqrt{|\alpha|}$, when the $\alpha$ becomes bigger than the critical value $\alpha_c$ at which WP pairs hit the Brillouin zone boundary and pair-annihilate, the system becomes a gapped insulator. According to the previous theoretical study [8], such a pair-creation and pair-annihilation process can be completed only within 1% variation of the $U/t$ ratio, where $t$ is the nearest-neighbor hopping amplitude. Thus the WSM phase can occupy a very narrow region of the phase diagram, which reflects the difficulty in approaching it in experiment.

## III. TOPOLOGICAL SEMIMETALS INDUCED BY ZEEMAN FIELD

On the other hand, when magnetic field is applied to the semimetal with QBC, various topological semimetals can emerge. The influence of the external Zeeman field $\vec{H}$ on QBC can be described by

$$\mathcal{H}_B = -\beta_1 \vec{B}\cdot\vec{J} - \beta_2 \vec{B}\cdot\vec{J}^3, \tag{2}$$

where $\vec{J} = (J_x, J_y, J_z)$, $\vec{J}^3 = (J_x^3, J_y^3, J_z^3)$, and $\vec{B} = \vec{B}(\vec{H}, \vec{M}, \ldots)$ indicates the effective Zeeman field including $\vec{H}$ and the average magnetization $\vec{M}$. Two constants $\beta_1$ and $\beta_2$ measure the magnitude of the isotropic and anisotropic Zeeman terms, respectively. The anisotropic Zeeman term coupled with the cubic invariant $\vec{J}^3$ arises due to spin-orbit coupling and the large total angular momentum $J = 3/2$. Normally, the anisotropic Zeeman term, which has been known as the $q$ term in the Luttinger Hamiltonian, is proportional to spin-orbit coupling and makes a tiny contribution to Zeeman splitting [25,26]. However, in pyrochlore iridates, it can make a significant contribution to the energy splitting at the Γ point whose magnitude can even be controlled by modulating the orientation of spins within a unit cell as explained below.

In general, the isotropic Zeeman term splits the degenerate eigenstates carrying different $J_z$, leading to equally spaced energy levels at the Γ point as shown in Fig. 3(b). Thus in systems with $\beta_1 \neq 0$ and $\beta_2 = 0$, Zeeman field $\vec{H}$ cannot make a level crossing between the states with different $J_z$ at the Γ point. On the other hand, when the isotropic and anisotropic Zeeman terms exist simultaneously, the energy ordering between states with different $J_z$ can be rearranged depending on the ratio $\beta_2/\beta_1 = \tan\theta$. Figure 4(a) shows the evolution of energy levels at the Γ point as $\theta$ varies when $\vec{H} \parallel [001]$. One can clearly see the level crossing at several critical angles $\theta_c$ which indicates topological phase transitions between different topological semimetals. As shown in Fig. 4(a), when $\vec{H} \parallel [001]$, one can obtain either a double Weyl semimetal (DWSM) having two WPs with the monopole charge ±2 on the $k_z$ axis or a line-node semimetal (LSM) having a circular nodal line on the $k_z = 0$ plane with two additional WPs on the $k_z$ axis. On the other hand, when $\vec{H} \parallel [111]$, since the residual symmetry of the system is lower than the case with $\vec{H} \parallel [001]$, band crossing at Γ can occur in a more limited situation; thus the resulting topological phase diagram is simpler as detailed in A.

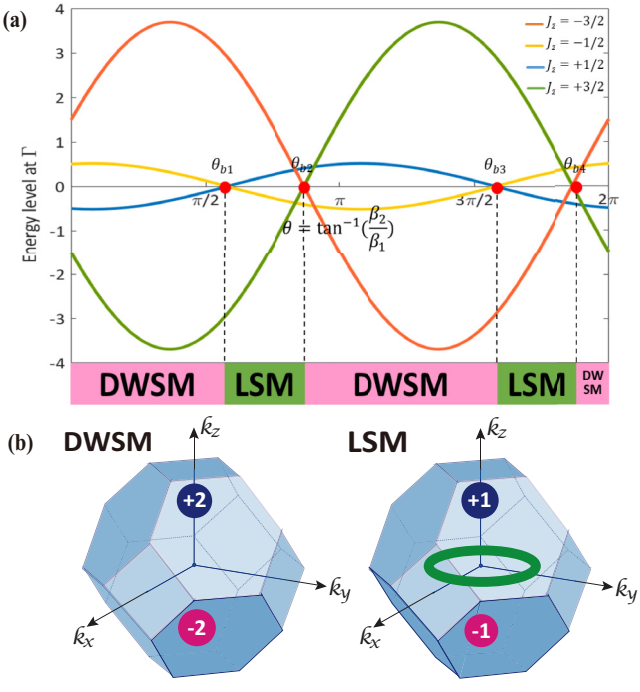


FIG. 4. (a) Change of energy levels at the Γ point when $\theta = \tan^{-1}[\beta_2/\beta_1]$ varies, and the associated phase diagram. Here we assume $\hbar = 1$ and plot the energy per unit magnetic field $E/B$. DWSM (LSM) denotes a double Weyl semimetal (a line-node semimetal). (b) Distribution of point/line nodes in DWSM and LSM.

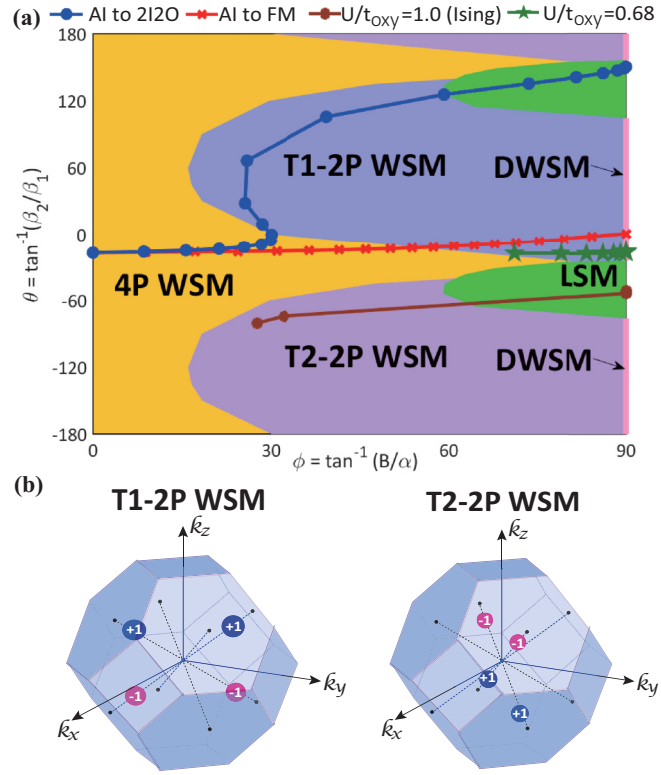


FIG. 5. (a) General phase diagram under magnetic field along [001] in the $(\theta, \phi)$ plane obtained from the extended Luttinger model. Here 4P WSM indicates a WSM with four pairs of WPs whereas T1-2P WSM (T2-2P WSM) denotes type-1 (type-2) WSM with two pairs of WPs. The solid lines indicate the trajectory followed by the mean-field lattice model when the spin orientation in a unit cell changes. (b) Distribution of WPs in T1/T2-2P WSM.

When magnetic field is applied to real materials, both AIAO ordering and two Zeeman terms exist simultaneously. Then the most general low-energy band structure can be captured by the extended Luttinger model $\mathcal{H}_{\text{extended}} \equiv \mathcal{H}_0 + \mathcal{H}_{\text{AIAO}} + \mathcal{H}_{\text{B}}$. Since there are three competing energy scales $\alpha, \beta_1, \beta_2$, one can obtain the general phase diagram in the two-dimensional $(\theta, \phi)$ plane where the angular variable $\phi \equiv \tan^{-1}(B/\alpha)$ is introduced to measure the importance of the Zeeman term relative to the energy scale for the AIAO ordering. As shown in Fig. 5(a), various novel topological semimetal phases can arise by tuning $\theta$ and $\phi$.

## IV. LATTICE MODEL AND CLUSTER MAGNETIC MULTIPOLE MOMENTS

To provide a microscopic picture for magnetic field induced topological semimetals in lattice systems, we study a tight-binding Hamiltonian $H = H_0 + H_U + H_Z + H_{fd}$, where $H_U = U \sum_i n_{i\uparrow} n_{i\downarrow}$ is the on-site Hubbard interaction, $H_Z = \sum_{i,s} c^\dagger_{i,s} \frac{(\vec{H}\cdot\vec{\sigma}_{ss'})}{2} c_{i,s'}$ indicates the Zeeman coupling, and $H_{fd}$ denotes the exchange coupling between Ir and Nd moments. $c_{i,s}$ ($c^\dagger_{i,s}$) is the annihilation (creation) operator for electrons carrying spin $s = \uparrow, \downarrow$ on the $i$th site, and $n_{is} = c^\dagger_{i,s} c_{i,s}$ is the electron number operator. Here it is assumed that each Ir ion carries an effective spin-1/2 moment represented by the Pauli matrix $\vec{\sigma}$. The hopping process between Ir sites is described by

$$H_0 = \sum_{s,s'} \Bigg[ \sum_{\langle ij \rangle} c^\dagger_{i,s} (t_1 + i t_2 \vec{d}_{ij} \cdot \vec{\sigma}_{ss'}) c_{j,s'} + \sum_{\langle\langle ij \rangle\rangle} c^\dagger_{i,s} (t'_1 + i\{t'_2 \vec{R}_{ij} + t'_3 \vec{D}_{ij}\} \cdot \vec{\sigma}_{ss'}) c_{j,s'} \Bigg], \quad (3)$$

where $t_1$ ($t'_1$) denotes the spin-independent hopping amplitude between nearest-neighbor (next-nearest-neighbor) sites, and $t_2$, $t'_{2,3}$ indicate spin-dependent hopping amplitudes including the oxygen-mediated hopping amplitude $t_{\text{oxy}}$ as well as the direct hopping amplitudes between Ir ions [8,12]. The Hubbard interaction term is treated by mean-field theory ($H_U \approx H_U^{\text{MF}}$) by introducing local order parameters $\vec{m}_\alpha \equiv \frac{1}{2N} \sum_{\boldsymbol{k}} \langle c^\dagger_{\alpha,s}(\boldsymbol{k}) \vec{\sigma}_{s,s'} c_{\alpha,s'}(\boldsymbol{k}) \rangle$ where $\alpha = 1, 2, 3, 4$ indicates the four spins within a unit cell. For $H_{fd}$, Nd moments are treated classically. (See Appendix D.)

Figure 6(a) shows the band structure of PM obtained by solving $H_0$. One can clearly see the presence of a QBC at the $\Gamma$ point that can be effectively described by the Luttinger Hamiltonian discussed before. To understand the nature of the four degenerate states at the QBC carrying $J = 3/2$, we have depicted the relevant wave functions in Fig. 6(a). One intriguing property of these degenerate eigenstates is that they intrinsically carry cluster magnetic multipole moments (CMMMs) defined below. Namely, the states with the angular momentum $J_z = \pm 3/2$ carry cluster magnetic dipole moments whereas the other two states with $J_z = \pm 1/2$ carry cluster magnetic dipole and octupole moments. Due to this intrinsic CMMM, those four states can selectively couple to

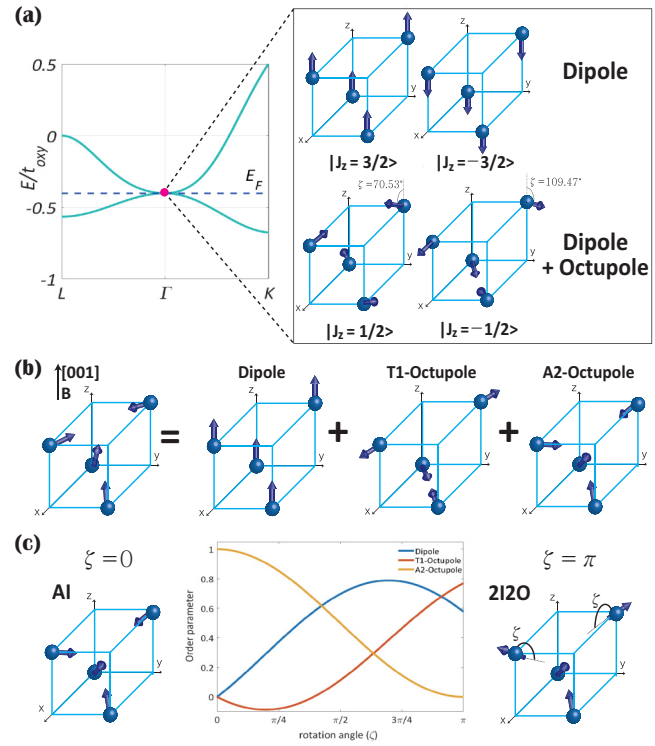


FIG. 6. (a) Description of the wave functions for the four degenerate states at QBC. (b) Decomposition of a generic spin configuration of a unit cell under $H \parallel [001]$ into magnetic multipole components. (c) Variation in the amplitude of each multipolar component as the spin structure in a unit cell is modulated from AI to 2I2O form under $H \parallel [001]$.

specific magnetic ordering patterns of a magnetically ordered phase.

The MMMs for a cluster of atoms have recently been introduced by Suzuki *et al.* in Ref. [27]. Analogously to the local multiple moment of an atom [28], the rank-$p$ MMM of a given cluster $\mu$ is defined as $M^\mu_{pq} = \sqrt{\frac{4\pi}{2p+1}} \sum_{i=1}^N \vec{m}_i \cdot \nabla_i (|R_i|^p Y^*_{pq}(\theta_i, \phi_i))$ where $q$ is the magnetic quantum number ranging from $-p$ to $p$, $N$ is the number of atoms in a cluster, $\vec{m}_i$ is the magnetic moment vector at the $i$th atom of the cluster, $(R_i, \theta_i, \phi_i)$ are the spherical coordinates of the $i$th atom, and $Y_{pq}$ is the spherical harmonics. By taking summation over all clusters in the magnetic unit cell, the $p$th order of the CMMM can be obtained.

The CMMM of a tetrahedral unit cell can be analyzed further as follows. Counting the three components of a spin separately, the twelve independent spin degrees of freedom in a unit cell can be classified by using group theory. The resulting symmetrized spin configuration with a fixed CMMM can be taken as a basis to represent the general spin configuration in a unit cell. For instance, when $\vec{H} \parallel [001]$, the most general configuration of the four spins in a unit cell satisfying the lattice symmetry $C_{2z}$ and $\sigma_d T$ can be written as

$$|\psi\rangle_{[001]} = a_D |D\rangle + a_{T_1} |T_1\rangle + a_{A_2} |A_2\rangle, \quad (4)$$

where $|D\rangle$, $|T_1\rangle$, $|A_2\rangle$ represent the basis states carrying cluster magnetic dipole, $T_1$-octupole, and $A_2$-octupole

moments, respectively, and $a_D$, $a_{T_1}$, $a_{A_2}$ represent the relevant amplitudes. [See Fig. 6(b).] Changing the spin orientations, $a_D$, $a_{T_1}$, $a_{A_2}$ can be tuned continuously as shown in Fig. 6(c).

Now let us describe how the intrinsic CMMMs of the four degenerate states at the QBC couple to the CMMM of a magnetically ordered phase. To understand the relation between the CMMM of a lattice system and the three magnetic terms $\alpha$, $\beta_1$, $\beta_2$ of the extended Luttinger Hamiltonian, one can project the effective Zeeman term $H_B = \frac{1}{2}\sum_{i,s} \vec{B}_{\text{eff},i} \cdot [c^\dagger_{i,s}\vec{\sigma}_{ss'}c_{i,s'}]$ to the subspace spanned by the four degenerate states at QBC. Here the local effective magnetic field $\vec{B}_{\text{eff},i}$ includes the influence of all interaction terms within the mean-field theory, and should be determined self-consistently for given $\vec{H}, U, J_{fd}$, and hopping parameters. By using the projection operator $\hat{P}_J = \sum_{J_z} |J_z\rangle\langle J_z|$ where $|J_z\rangle$ indicates the four degenerate states at QBC with the angular momentum $J_z$,

$$\hat{P}_J H_B \hat{P}_J = M_{A_2}\Gamma_{45} + \left[\tfrac{2}{3}M_D - \tfrac{9}{4}M_{T_1}\right]J_z + M_{T_1}J_z^3 \qquad (5)$$

for the [001] field, where $M_{A_2}$, $M_D$, $M_{T_1}$ indicate the $A_2$-octupole moment (or AIAO order parameter), the magnetic dipole moment (or magnetization), and the $T_1$-octupole moment, respectively. It is worth noting that $M_D$ and $M_{T_1}$ determine the relative importance between the isotropic and anisotropic Zeeman terms. Since the CMMMs determine the three magnetic terms $\alpha$, $\beta_1$, $\beta_2$, one can expect that various topological semimetals predicted by the extended Luttinger model can be realized simply by changing the spin directions that control the CMMMs.

To demonstrate this idea, we have determined $\alpha$, $\beta_1$, $\beta_2$ by projecting the lattice model for various processes of changing spin orientations, and plotted the relevant trajectories in Fig. 5(a). For instance, the red (blue) line in Fig. 5(a) describes the trajectory when the effective Zeeman field $\vec{B}_{\text{eff},i}$ rotates the spins in a unit cell continuously from the AIAO configuration to the collinear ferromagnetic (2-in 2-out) state. Depending on how the spin orientation changes, the CMMM of the unit cell and $\alpha$, $\beta_1$, $\beta_2$ change differently, which results in distinct trajectories and associated topological semimetals.

In real materials, the spin modulation pattern under magnetic field depends strongly on the microscopic parameters determining $\vec{B}_{\text{eff,i}}$ in self-consistent calculations. Figure 7 shows two phase diagrams in the $(H, U)$ plane determined by self-consistent mean-field theory. Depending on whether Ir spins are treated as an Ising spin or a Heisenberg spin, we obtain different phase diagrams including distinct topological semimetals. In both cases, however, the origin of emergent topological semimetals can be understood based on Fig. 5(a). For instance, the mean-field Hamiltonian projected along the brown (green) horizontal line in the left (right) figure in Fig. 7 gives the brown (green) trajectory in Fig. 5(a), demonstrating the origin of the relevant topological semimetals. This shows that various emergent topological semimetals can be successfully described by the QBC of the PM coupled to competing magnetic energy scales $\alpha$, $\beta_1$, $\beta_2$ in the extended Luttinger model.

Up to now, we have considered only Nd, which is a Kramers ion, for the description of $fd$-exchange coupling. However, the role of the non-Kramers ion Pr should be properly taken into account for the application of our theory to $(Nd_{1-x}Pr_x)_2Ir_2O_7$ near the QCP. Due to the distinct symmetry properties of Nd and Pr pseudospins, the form of $fd$-exchange coupling is also quite different in the two cases [29]. For instance, the in-plane components of the pseudospin operators are time-reversal-invariant quadrupoles for $Pr^{3+}$ whereas they are time-reversal odd dipole-octupoles for $Nd^{3+}$[30]. As a result, Pr in-plane spin components couple to Ir charge density instead of Ir spin density [31]. (See Appendix D.) However, such a variation in the $fd$-exchange coupling can at most modify the trajectory that the system follows under magnetic field, which can be captured in the variation of $\alpha$, $\beta_1$, $\beta_2$ in the extended Luttinger Hamiltonian. The global structure of the phase diagram should remain invariant as summarized in Fig. 5(a).

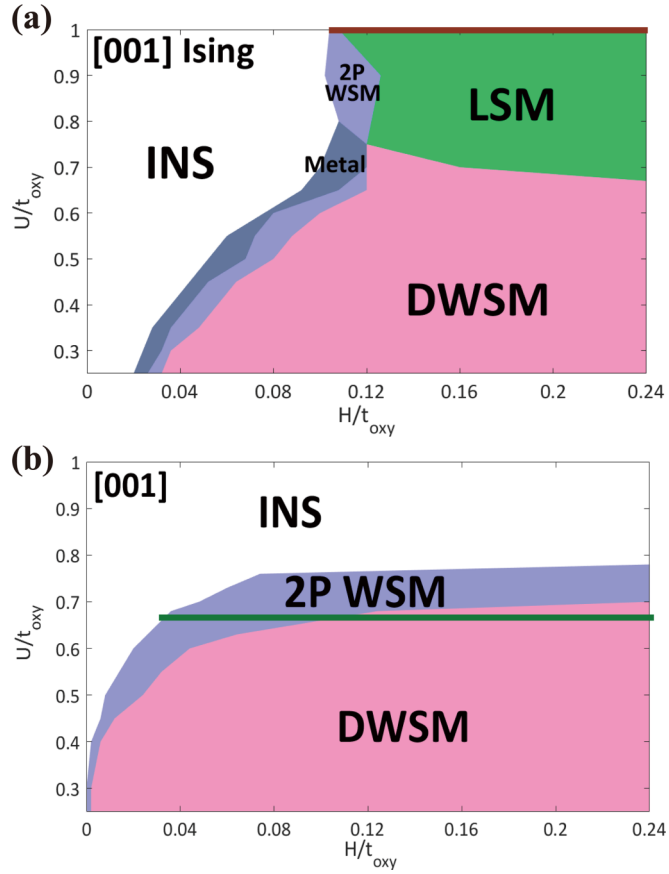


FIG. 7. Phase diagrams from self-consistent mean-field theory when Ir is treated as an Ising spin (a) or as a Heisenberg spin (b). The horizontal brown (green) solid line in (a) [(b)] corresponds to the brown (green) curve in Fig. 5(a). $\alpha$, $\beta_1$, and $\beta_2$ of the relevant effective Hamiltonian are calculated by using the projection matrix in Eq. (5).

## V. CONCLUSIONS

We have shown that magnetic field induced topological semimetals near the QCP can be understood based on the band structure near the $\Gamma$ point. In systems located away from the QCP, however, one needs to consider accidental band crossings away from the $\Gamma$ point, which changes the total

number of WPs. For instance, the influence of band crossings at the $L$ point is shown in Appendix B.

Since the presence of QBC near the Fermi level is the key ingredient for the field induced topological semimetals summarized in Fig. 5(a), the same idea can be applied to a broad class of materials having a similar low-energy band structure, such as HgTe [32] or GdPtBi [23]. However, it is worth noting that the noncoplanar magnetic structure of pyrochlore iridates plays a critical role in enlarging the anisotropic Zeeman term in the effective Hamiltonian because it is proportional to the cluster magnetic octupole moment as shown in Eq. (5). Since HgTe is a paramagnet and GdPtBi is a collinear antiferromagnet, the conventional linear Zeeman term should dominate over the Luttinger $q$ term in both materials, and thus the accessible topological semimetal phases are expected to be more limited.

Since the Pr doping necessarily introduces at least a weak disorder effect in the system, although the quality of the pyrochlore iridate samples synthesized recently is reasonably high, we discuss the influence of disorder on the phase diagram in Fig. 5(a). Let us note that because the applied magnetic field lowers the crystalline symmetry, all the topological semimetals shown in Fig. 5(a) develop small electron or hole pockets with the nodal points or lines located away from the Fermi level. As is well known in conventional metals, the weak disorder is an irrelevant perturbation, and thus its influence is negligible. Even if the Weyl points are accidentally located at the Fermi level, weak disorder is still marginally irrelevant according to the recent renormalization group analysis [35–38]. Although the disorder effect in a nodal line semimetal is more subtle [39], since the gap-closing points of a nodal line generally do not appear simultaneously at the Fermi level and additional small Fermi surfaces from Weyl points are present, we expect that the weak disorder is still irrelevant in the nodal line semimetal phase as well. Therefore we believe that the physics we have proposed remains valid even in the presence of weak disorder.

We conclude with discussing magnetic fluctuation effects near the QCP [33,34]. Poor screening of the Coulomb interaction in the semimetal with QBC is known to induce non-Fermi-liquid behavior and unusual magnetic quantum criticality associated with AIAO ordering. In the presence of magnetic field, however, broken cubic lattice symmetry allows the system to develop electron or hole pockets near Fermi energy $E_F$. In fact, all the topological semimetals shown in Fig. 5(a) possess a Fermi surface with nodal points or lines located near $E_F$. In this case, the magnetic transition of AIAO ordering is described by the conventional Hertz-Millis theory coupled to fermions with a Fermi surface. Examining the magnetic field induced crossover from non-Fermi-liquid physics to conventional Hertz-Millis type behavior and the influence of the bulk topological property on magnetic quantum criticality would be an interesting topic for future study.

## ACKNOWLEDGMENTS

T.O. was supported by the Institute for Basic Science in Korea (Grant No. IBS-R009-D1). H.I. was supported by JSPS KAKENHI Grants No. JP16H06717, No. JP18H03676, No. JP18H04222, and No. JP26103006, ImPACT Program of Council for Science, Technology and Innovation (Cabinet Office, Government of Japan), and CREST, JST (Grant No. JPMJCR16F1). B.-J.Y. was supported by the Institute for Basic Science in Korea (Grant No. IBS-R009-D1) and Basic Science Research Program through the National Research Foundation of Korea (NRF) (Grants No. 0426-20170012, No.0426-20180011), the POSCO Science Fellowship of POSCO TJ Park Foundation (No. 0426-20180002), and the US Army Research Office under Grant No. W911NF-18-1-0137. We thank N. Nagaosa for useful discussion.

## APPENDIX A: EFFECTIVE THEORY AT THE Γ POINT

### 1. Symmetry of pyrochlore iridates

Pyrochlore iridate $R_2Ir_2O_7$ (R-227) comprises two intertwined pyrochlore lattices of $R$ (rare-earth) and Ir ions. An octahedron with oxygen ions surrounds each Ir ion. Each pyrochlore lattice is composed of linked tetrahedra, in which two adjacent tetrahedra are inversion-symmetric about the linked point. Figure 1(a) shows the structure of pyrochlore iridates. A tetrahedron is the unit cell of the pyrochlore lattice. The structure of pyrochlore iridates is depicted in Fig. 1(a).

The point group of pyrochlore iridates is $T_d$ (tetrahedron), which contains 5 equivalent classes: identity ($\mathbb{I}$), threefold rotations ($C_3$), twofold rotations ($C_2$), diagonal mirrors ($\sigma_d$), and $\pi/2$ rotations followed by mirrors ($S_4$). Including spin-orbit coupling (SOC) in the system, we should utilize the $T_d$ double group in the argument. The $T_d$ double group has 8 equivalent classes, including identity ($\bar{\mathbb{I}}$), threefold rotations($\bar{C}_3$), and $\pi/2$ rotations followed by mirrors ($\bar{S}_4$) after $2\pi$ rotation. Accordingly, the number of $T_d$ double group representations is 8. Moreover, $\mathbb{P} \equiv \{P|T_{1/4,1/4,1/4}\}$ (space inversion and half translation), $T$ (time-reversal), and $T_r$ (FCC lattice translation) symmetries are preserved. The space group of pyrochlore iridates is $fd\bar{3}m$. Since we argue in momentum space, $\mathbb{P} \equiv P$ regardless of eigenvalues.

### 2. Luttinger Hamiltonian

We begin with quadratic band crossing in the paramagnetic semimetal phase of Pr-227 [9]. Since the magnetic ordering simultaneously occurs with the metal-insulator transition, we infer that magnetic ordering is the crucial source of band manipulation. Thus, we can assume, in general, that quadratic band crossing appears for the paramagnetic semimetal phase of pyrochlore iridates.

With $T$ and $P$ symmetry in the system, one needs at least $4 \times 4$ Hermitian matrices by Kramers degeneracy of each band. According to group theory, we should use $4 \times 4$ Hermitian matrices, since the largest dimension among the irreducible representations (irreps) of the $T_d$ double group is 4 ($\Gamma_8$ representation).

We can build the effective Hamiltonian by gathering the anticommuting matrices since such Hamiltonian gives only two distinct energy bands. The number of bases of the space of $4 \times 4$ Hermitian matrices is 16, but only 5 of them are anticommuting. Therefore, the effective Hamiltonian of quadratic

band crossing is

$$\mathcal{H}_0(\vec{k}) = \epsilon_0(\vec{k}) + \sum_{i=1}^{5} d_i(\vec{k})\Gamma_i, \tag{A1}$$

where $\epsilon_0(\vec{k}) = k^2/2m$, and $\Gamma_i$ are 5 anticommuting $4 \times 4$ matrices, $\{\Gamma_i, \Gamma_j\} = 2\delta_{ij}$. The algebra is called $SO(5)$ Clifford algebra. Explicitly,

$$\begin{aligned}
&\Gamma_1 = \frac{1}{\sqrt{3}}\{J_y, J_z\} = \tau_z\sigma_y, \quad \Gamma_2 = \frac{1}{\sqrt{3}}\{J_z, J_x\} = \tau_z\sigma_x,\\
&\Gamma_3 = \frac{1}{\sqrt{3}}\{J_x, J_y\} = \tau_y, \quad \Gamma_4 = \frac{1}{\sqrt{3}}\left(J_x^2 - J_y^2\right) = \tau_x,\\
&\Gamma_5 = J_z^2 - \frac{5}{4} = \tau_z\sigma_z,
\end{aligned} \tag{A2}$$

where $\tau_i$, $\sigma_i$ are Pauli matrices, and $J_i$ are spin-3/2 matrices. Also, the coefficients are defined as

$$\begin{aligned}
&d_1 = -\sqrt{3}ak_yk_z, \quad d_2 = -\sqrt{3}ak_zk_x, \quad d_3 = -\sqrt{3}ak_xk_y,\\
&d_4 = -\frac{\sqrt{3}}{2}b\left(k_x^2 - k_y^2\right), \quad d_5 = -\frac{1}{2}b\left(2k_z^2 - k_x^2 - k_y^2\right),
\end{aligned} \tag{A3}$$

where $a$, $b$ are arbitrary constants.

The Hamiltonian is called the Luttinger Hamiltonian [24]. Since we are only interested in the band crossings, we assume particle-hole symmetry and isotropy, for convenience. That is, we ignore the term $\epsilon_0(\vec{k})$ and let the coefficient $a = b = 1$. Furthermore, we concentrate on the band crossing between two middle bands, since we will assume half filling in the lattice model.

### 3. AIAO order parameter

As the neutron scattering experiment turned out, rare-earth or Ir moments in pyrochlore iridates form all-in all-out (AIAO) order [11], in which every magnetic moment points either to or from the center of the tetrahedron [Fig. 1(b)]. Accordingly, we should primarily include the AIAO order parameter in the theory. A pyrochlore lattice with AIAO order breaks $T$, $\sigma_d$, and $S_4$ symmetry, but preserves the combinations $\sigma_d T$ and $S_4 T$.

The AIAO order parameter transforms as the $\Gamma_2$ representation of the $T_d$ double group. Hence, we should add

$$\mathcal{H}_{\text{AIAO}} = -\alpha\Gamma_{45}, \tag{A4}$$

where $\Gamma_{ab} = [\Gamma_a, \Gamma_b]/2i$, and $\alpha$ is AIAO order parameter.

In the presence of AIAO order only, the effective Hamiltonian is

$$\mathcal{H}_{\text{eff},1} = \mathcal{H}_0 + \mathcal{H}_{\text{AIAO}}. \tag{A5}$$

The eigenenergy is

$$E_{\eta,\zeta} = \eta\sqrt{k^4 + \alpha^2 + 2\alpha\zeta\sqrt{d_1^2 + d_2^2 + d_3^2}}, \tag{A6}$$

where $\eta, \zeta = \pm 1$. $(\eta, \zeta\frac{|\alpha|}{\alpha}) = (+1, -1)$ and $(-1, -1)$ cross at eight Weyl points, $\vec{k} = \sqrt{|\alpha|/3}\ (\pm 1, \pm 1, \pm 1)$. The Weyl points stick on threefold-rotation-invariant ($[H, C_3] = 0$) axes, [111], [1$\bar{1}\bar{1}$], [$\bar{1}$1$\bar{1}$], and [$\bar{1}\bar{1}$1], for any $\alpha \neq 0$. According to the condition $C_3^3 = -1$, the threefold rotation operator can have three distinct eigenvalues, $e^{\pm i\pi/3}$ and $-1$, and two crossing bands have different eigenvalues among them. For example, for the band crossing along the [111] direction, the eigenvalues of crossing bands are $e^{-i\pi/3}$ and $-1$, respectively.

### 4. Effective field

Before arguing the topological phases under the effective field, we must note the remaining symmetries for each direction of the field.

If magnetic field is applied in the [001] direction without any magnetic order in the pyrochlore iridates, the symmetry operations are identity $I$, twofold rotation $C_{2z}$, twofold rotation followed by time reversal $C_{2x}T$, $C_{2y}T$, and the mirror symmetry about the plane including [001] followed by time-reversal $2\sigma_{d,001}T$, $\pi/2$ rotation followed by the mirror $S_{4z}$, and inversion ($P$). There is also a combined symmetry $M_z = C_{2z}P$, which acts as mirror symmetry only in momentum space, since $P$ is inversion with half translation in real space. If we apply the [001] direction field with AIAO order of the magnetic moment, there are only $I$, $C_{2z}$, $2\sigma_{d,001}T$, $P$, and $\mathcal{M}_z$.

If magnetic field is applied in the [111] direction without any magnetic order in the pyrochlore iridates, the symmetry operations are identity $I$, threefold rotation around the [111] line $C_{3,111}$, mirrors through the plane including [111] followed by time-reversal $3\sigma_{d,111}T$, and inversion $P$. If we apply the [111] direction field with AIAO order of magnetic moment, still $I$, $C_{3,111}$, $3\sigma_{d,111}T$, and $P$ are preserved.

The magnetic field transforms as the $\Gamma_4$ representation of the $T_d$ double group, so the following terms are allowed:

$$\mathcal{H}_B = -\beta_1\vec{B}\cdot\vec{J}_1 - \beta_2\vec{B}\cdot\vec{J}_3, \tag{A7}$$

where $\vec{B}(\vec{H}, \vec{M}, \ldots)$ is the effective magnetic field, which is the function of magnetic field $\vec{H}$ and magnetization $\vec{M}$, and other order parameters which transform the same as magnetic field and magnetization:

$$\mathcal{H}_{\text{eff},2} = \mathcal{H}_0 + \mathcal{H}_B. \tag{A8}$$

By diagonalizing $\mathcal{H}_{\text{eff},2}$, we can observe topological phases when the AIAO order parameter is trivial.

Although $\mathcal{H}_{\text{eff},2}$ is too complicated to obtain the energy spectrum in an analytic way, we can acquire the energy spectrum along high-symmetry lines and on the mirror planes. Let us consider the [001] effective field first. Then, Eq. (A7) becomes

$$\mathcal{H}_{B,001} = -B\left(\cos\theta J_z + \sin\theta J_z^3\right), \tag{A9}$$

where $\beta_1 = \cos\theta$, $\beta_2 = \sin\theta$. $\theta$ is the variable that controls the relative magnitude of the Zeeman and Luttinger $q$ term. Since there is $C_{2z}$ and $\mathcal{M}_z = C_{2z}P$ symmetry, we investigate along the $k_z$ axis and $k_z = 0$ plane.

Along the $k_z$ axis, the Hamiltonian becomes

$$\mathcal{H}_{001} = d_5(k_z)\Gamma_5 + \mathcal{H}_{B,001}, \tag{A10}$$

because $d_{1,2,3,4} = 0$ when $k_x = k_y = 0$. Since the Hamiltonian is already diagonalized on the basis of $J_z = \pm 3/2, \pm 1/2$,

the energy spectrum is just

$$\begin{aligned} E_{3/2} &= k_z^2 - B\left(\tfrac{3}{2}\cos\theta + \tfrac{27}{8}\sin\theta\right), \\ E_{-3/2} &= k_z^2 + B\left(\tfrac{3}{2}\cos\theta + \tfrac{27}{8}\sin\theta\right), \\ E_{1/2} &= -k_z^2 - B\left(\tfrac{1}{2}\cos\theta + \tfrac{1}{8}\sin\theta\right), \\ E_{-1/2} &= -k_z^2 + B\left(\tfrac{1}{2}\cos\theta + \tfrac{1}{8}\sin\theta\right). \end{aligned} \tag{A11}$$

According to the energy spectrum at $\Gamma$, the band crossings of two middle bands will change as varying $\theta$.

Defining $a \equiv \frac{3}{2}\cos\theta + \frac{27}{8}\sin\theta$ and $b \equiv \frac{1}{2}\cos\theta + \frac{1}{8}\sin\theta$, we can divide into 4 cases, where $a$ and $b$ are either positive or negative, respectively. Note that $\mu_i$ are Pauli matrices, $B$ is positive, and $\theta$ ranges from 0 to $2\pi$.

(1) $a > 0, b > 0$. If $\theta < \pi - \arctan 4 = \theta_{b1}$ or $\theta > 2\pi - \arctan\frac{4}{9} = \theta_{b4}$, then $a > 0, b > 0$. $E_{3/2}$ and $E_{-1/2}$ are two middle bands, and cross at two points. Concentrating on two crossing bands, we induce

$$\begin{aligned} \mathcal{H}_{1,2\times 2} = &\frac{-a+b}{2}\mu_0 + \frac{-a-b}{2}\mu_z + d_3(\vec{k})\mu_y \\ &+ d_4(\vec{k})\mu_x + d_5(\vec{k})\mu_z. \end{aligned} \tag{A12}$$

A pair of double Weyl points emerge according to the $d$-wave nature of $d_3$ and $d_4$.

(2) $a < 0, b < 0$. If $\pi - \arctan\frac{4}{9} = \theta_{b2} < \theta < 2\pi - \arctan 4 = \theta_{b3}$, then $a < 0, b < 0$. $E_{-3/2}$ and $E_{1/2}$ are two middle bands, and cross at two points. The two-band projected theory is

$$\begin{aligned} \mathcal{H}_{2,2\times 2} = &\frac{a-b}{2}\mu_0 + \frac{-a-b}{2}\mu_z + d_3(\vec{k})\mu_y \\ &+ d_4(\vec{k})\mu_x - d_5(\vec{k})\mu_z. \end{aligned} \tag{A13}$$

For the same reason as the first case, a couple of double Weyl points appear.

(3) $a > 0, b < 0$. When $\theta_{b1} < \theta < \theta_{b2}$, we have $a > 0, b < 0$. $E_{3/2}$ and $E_{1/2}$ are two middle bands, and cross at two points. Two crossing bands are written as

$$\begin{aligned} \mathcal{H}_{3,2\times 2} = &\frac{-a-b}{2}\mu_0 + \frac{-a+b}{2}\mu_z + d_1(\vec{k})\mu_y \\ &+ d_2(\vec{k})\mu_x + d_5(\vec{k})\mu_z. \end{aligned} \tag{A14}$$

In this case, $d_1$ and $d_2$ have $p$-wave nature, so a pair of single Weyl points emerge.

(4) $a < 0, b > 0$. If $\theta_{b3} < \theta < \theta_{b4}$, we have $a < 0, b > 0$. $E_{-3/2}$ and $E_{-1/2}$ are two middle bands, and cross at two points. Projecting on two crossing bands, we have

$$\begin{aligned} \mathcal{H}_{4,2\times 2} = &\frac{a+b}{2}\mu_0 + \frac{-a+b}{2}\mu_z - d_1(\vec{k})\mu_y \\ &- d_2(\vec{k})\mu_x - d_5(\vec{k})\mu_z. \end{aligned} \tag{A15}$$

Likewise, there are a couple of single Weyl points.

To sum up, along the $k_z$ axis, $\theta$ determines the emergence of either a pair of double Weyl or single Weyl points. All of them stick at the $k_z$ axis by twofold rotation symmetry $C_{2z}$, whose possible eigenvalues are $\pm i$. The eigenvalues of the twofold rotation operators of the crossing bands are equal for double Weyl, but opposite for single Weyl points. These points are topologically protected; even though twofold rotation symmetry is broken, Weyl points are not annihilated immediately.

Meanwhile, on the $k_z = 0$ plane, the Hamiltonian becomes

$$\mathcal{H}_{k_z=0}(\vec{k}) = d_3(\vec{k})\Gamma_3 + d_4(\vec{k})\Gamma_4 + d_5(\vec{k})\Gamma_5 + \mathcal{H}_{B,001}, \tag{A16}$$

where $\vec{k} = (k_x, k_y, 0)$. The plane is invariant under $\mathcal{M}_z = C_{2z}P$; that is, $\mathcal{M}_z^\dagger H_{k_z=0}(k_x, k_y, 0)\mathcal{M}_z = H_{k_z=0}(-k_x, -k_y, 0) = H_{k_z=0}(k_x, k_y, 0)$. Diagonalizing the matrix, we get the energy spectrum

$$\begin{aligned} E_{\eta,\zeta} = &\eta\sqrt{d_3^2 + d_4^2 + \left[d_5 - \zeta B\left(\cos\theta + \frac{7}{4}\sin\theta\right)\right]^2} \\ &- \zeta B\left(\frac{1}{2}\cos\theta + \frac{13}{8}\sin\theta\right), \end{aligned} \tag{A17}$$

where $\eta, \zeta = \pm 1$. $-i\zeta$ is an eigenvalue of $\mathcal{M}_z$. In order to detect band crossings, let us define $c \equiv (\frac{1}{2}\cos\theta + \frac{13}{8}\sin\theta)$ and $d \equiv |\cos\theta + \frac{7}{4}\sin\theta|$. Since $B$ and $d$ are positive-definite, we divide the case according to the sign of $c$.

To observe crossing points, we should consider two aspects: the $\mathcal{M}_z$ eigenvalue of each band and energy level at $\Gamma$. Two crossing bands should have different eigenvalues of $\mathcal{M}_z$, either $-i$ or $+i$. In addition, the lowest/highest part of the crossing band which appears at $\Gamma$ should be in the negative/positive energy level, since energy increases/decreases monotonically when departing from $\Gamma$.

(1) When $c > 0$, the crossings between $E_{1,1}$ and $E_{-1,-1}$ emerge only if $c - d > 0$, where $\mp(c - d)$ is the $\Gamma$-point energy of each band. The $\mathcal{M}_z$ eigenvalue of $E_{1,1}$ and $E_{-1,-1}$ is $-i$ and $+i$, respectively. Surprisingly, the range of $\theta$ satisfying $c - d > 0$ is $\theta_{b1} < \theta < \theta_{b2}$, which is the range of $a > 0, b < 0$.

(2) When $c < 0$, the crossings between $E_{1,-1}$ and $E_{-1,1}$ emerges only if $c + d < 0$, where $\pm(c + d)$ is the $\Gamma$-point energy of each band. Likewise, the $\mathcal{M}_z$ eigenvalue of $E_{1,-1}$ and $E_{-1,1}$ is $+i$ and $-i$, respectively. The range of $\theta$ satisfying $c + d < 0$ is $\theta_{b3} < \theta < \theta_{b4}$, which is consistent with the range of $a < 0, b > 0$.

We infer that the crossings on the $k_z = 0$ plane coexist with a pair of single Weyl points on the $k_z$ axis, and are protected by $\mathcal{M}_z$ symmetry.

$\mathcal{M}_z$ symmetry makes a line node form crossing on the $k_z = 0$ plane. For example, for the $c > 0$ case, the crossing occurs when

$$k_x^2 + k_y^2 = 2\frac{\sqrt{c^2(4c-d)(c-d)}}{d^2 - 4c^2}. \tag{A18}$$

This is nothing but a circle. The term inside the square root can only be positive if $c - d > 0$. With a similar argument, we also have a line node for the $c < 0$ case.

In short, with the [001] effective field, we observe two available crossings: (i) a pair of double Weyl points along the $k_z$ axis (double Weyl semimetal, DWSM); (ii) a pair of single Weyl points along the $k_z$ axis with a line node on the $k_z = 0$ plane (line node semimetal, LSM). Crossing points at the $k_z$ axis are topologically protected, while a line node on the $k_z = 0$ plane is protected by $\mathcal{M}_z$ symmetry. With only the Zeeman term, we find no additional level crossing between

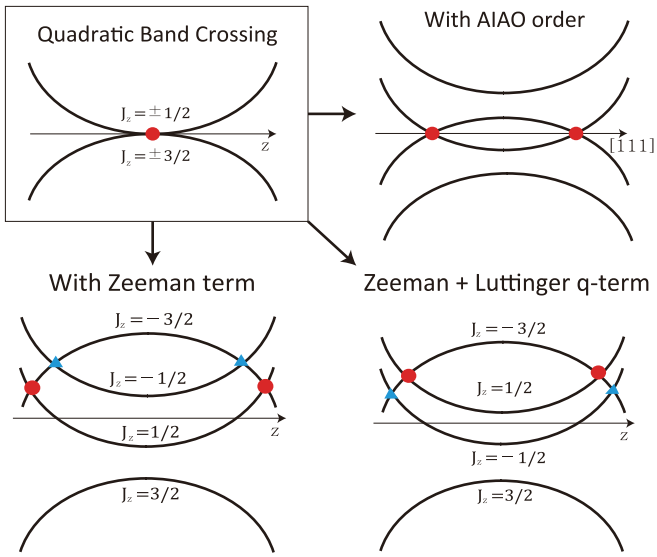


FIG. 8. The role of the AIAO order parameter, Zeeman term, and Luttinger $q$ term in quadratic band crossing. Only with the AIAO or Zeeman term, we find no additional level crossing between 4 degenerate eigenstates at the Γ point. However, with both the Zeeman and Luttinger $q$ term, additional level crossing can occur.

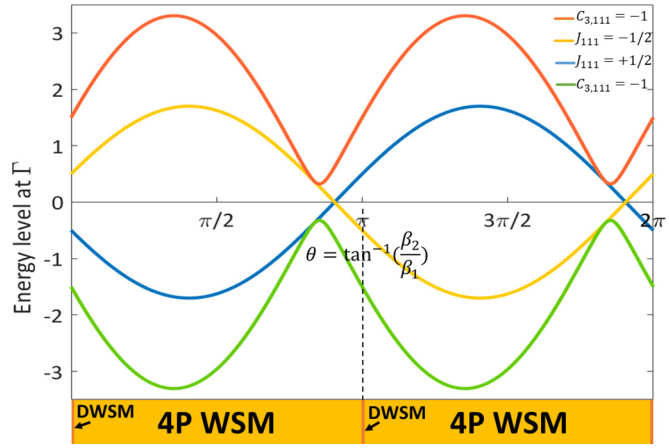


FIG. 9. The energy spectrum at the Γ point as a function of $\theta = \tan^{-1}\beta_2/\beta_1$ is drawn for the [111] field. We suppose the angular momentum unit to be 1, and apply the unit effective Zeeman field like in Fig. 4. The Hamiltonian is diagonalizable with $C_{3,111}$ eigenstates instead of $J_{[111]}$ eigenstates. As the top and bottom energy level share the $C_{3,111}$ eigenvalue, they cannot cross as $\theta$ changes, unlike the [001] field.

4 degenerate eigenstates, while in the presence of the Zeeman and Luttinger $q$ term, additional level crossing can occur. (See Figs. 3 and 8.)

Next, with the [111] effective field, the Hamiltonian is

$$\mathcal{H}_{B,111} = -\frac{B}{\sqrt{3}}\left[\cos\theta(J_x + J_y + J_z) + \sin\theta\left(J_x^3 + J_y^3 + J_z^3\right)\right]. \tag{A19}$$

Even on the high-symmetry line [111], notwithstanding, it is too complicated to acquire the energy spectrum analytically. The Hamiltonian cannot be diagonalized under the basis that $J_{111} = \pm\frac{3}{2}, \pm\frac{1}{2}$, since $(J_x + J_y + J_z)$ and $(J_x^3 + J_y^3 + J_z^3)$ do not commute. In spite of the complexity, we can still investigate the Γ-point energy spectrum to acquire the nature of crossing points between two middle bands on the [111] line, where threefold rotational symmetry is preserved.

In Fig. 9, four energy levels at the Γ point have been drawn against $\theta$. At any $\theta$, we can label the energy level at Γ with eigenvalues of $C_{3,111} = e^{i\frac{2\pi}{3\sqrt{3}}(S_x+S_y+S_z)}$, threefold rotation around the [111] line. Comparing the $C_{3,111}$ basis with the $J_{[111]}$ eigenstates, we confirm that $J_{[111]} = \pm 1/2$ corresponds to two middle energy levels for every $\theta$, and the other two energy levels are the linear combination of $J_{[111]} = \pm 3/2$. From $C_{3,111}^3 = -1$, we observe that $J_{[111]} = \pm 1/2$ have the eigenvalue of $e^{\mp i\pi/3}$, and $J_{[111]} = \pm 3/2$ states have eigenvalue $-1$. Since the number of energy bands is larger than the number of possible eigenvalues of $C_{3,111}$, it is natural to have two energy levels whose eigenvalues of $C_{3,111}$ are identical. Furthermore, since $J_{[111]} = \pm 3/2$ have the same eigenvalue of $C_{3,111}$, the hybridization of $J_{[111]} = \pm 3/2$ is inevitable.

We label the energy band as $E_{-1,\text{top}}$, $E_{-1,\text{bot}}$, $E_{\pm 1/2}$, whose energy level at Γ is in Fig. 9. We consider the $0 \leqslant \theta < \pi$ range primarily, since $\pi \leqslant \theta < 2\pi$ will be similar. The band crossing occurs between $E_{-1,\text{top}}$ and $E_{1/2}$ for $\theta < \pi - \arctan\frac{4}{13} \sim 2.84309 = \theta_{c2}$, and between $E_{-1,\text{top}}$ and $E_{-1/2}$ otherwise. Meanwhile, the $E_{-1,\text{top}}$ band changes its component from $J_{[111]} = -3/2$ to $3/2$, when $\theta$ varies from 0 to $\pi$. Especially, $J_{[111]} = \pm 3/2$ states are significantly mixed near $\theta_{c1} = \pi - \frac{1}{2}\arctan(\frac{184}{139}) \sim 2.67968$. The band crossings between $E_{-1,\text{top}}$ and $E_{1/2}$ are double Weyl nodes only if $\theta = 0$, since $J_{[111]} = \pm 3/2$ becomes the eigenstates of the Hamiltonian. Otherwise, each double Weyl node is broken into 4 single Weyl nodes. According to the conservation of topological charge, one of 4 single Weyl nodes has the opposite topological charge of the rest of the single Weyl nodes.

To sum up, band crossings along the [111] direction are double Weyl points at $\theta = 0$ where $J_{[111]} = -\frac{3}{2}, \frac{1}{2}$ states cross, and immediately break into single Weyl points as $\theta$ increases because of the hybridization of $J_{[111]} = \pm 3/2$ states. In fact, observing crossing points numerically, one can locate 4 pairs of single Weyl points including a pair on the [111] axis. Similarly, band crossings become double Weyl points at $\theta = \pi$, because $J_{[111]} = \frac{3}{2}, -\frac{1}{2}$ cross.

So far, we suggest various topological phases of pyrochlore iridates only under the effective field, by virtue of the interplay between the Zeeman and Luttinger $q$ term. For the [001] direction, a double Weyl semimetal (DWSM) and a line-node semimetal (LSM) emerge. For the [111] direction, a DWSM and 4-pair Weyl semimetal (4P WSM) appear.

### 5. AIAO and effective field

In this section, we take both the AIAO order parameter and effective field into account simultaneously.

Given the large AIAO order parameter and weak effective field strength, we draw trajectories of the crossing points through the perturbation theory near each Weyl point. In addition, we investigate the emergence of crossing points between two middle bands by the perturbation theory near Γ, and establish the phase diagram with two variables: $\theta$,

controlling the ratio between the Zeeman and Luttinger $q$ term, and $\phi$, controlling the ratio between the AIAO order parameter and effective field strength ($\tan\phi = B/\alpha$).

#### *a. [001] direction*

Let us begin from the [001] direction. There are 8 Weyl points if AIAO order exist, and all of them stick on the threefold rotation axis. Since the [001] magnetic field breaks all of the threefold rotation symmetries, every Weyl point will move away from the rotation axes. Given the mirror symmetry $2\sigma_{d,001}$ and the topological nature, the Weyl points will travel on the mirror plane whose normal vector is either [110] or [1$\bar{1}$0]. If the Weyl points travel out of the plane, each Weyl node should divide into two by mirror symmetry, and then the Nielsen-Ninomiya theorem is violated.

According to the symmetries, we can divide 8 Weyl fermions into 2 classes: class 1, 4 Weyl points included in the mirror plane with the [1$\bar{1}$0] normal vector, and class 2, the other 4 Weyl points included in the mirror plane with the [110] normal vectors.

If we choose one of the class 1 Weyl points at $\vec{k}_{C1,001} = \sqrt{\frac{\alpha}{3}}(1, 1, 1)$, the Hamiltonian near the point $\vec{k} = \vec{k}_{C1,001} + \vec{q}$ becomes

$$\mathcal{H}^{001}_{C1} = \mathcal{H}^{001}_{0,C1} + \mathcal{H}^{001}_{\mathrm{mom},C1}, \tag{A20}$$

where

$$\mathcal{H}^{001}_{0,C1} = -\frac{\alpha}{\sqrt{3}}(\Gamma_1 + \Gamma_2 + \Gamma_3) - \alpha\Gamma_{45}, \tag{A21}$$

$$\begin{aligned}\mathcal{H}^{001}_{\mathrm{mom},C1} = &-\sqrt{\alpha}\Big[(q_y + q_z)\Gamma_1 + (q_z + q_x)\Gamma_2 \\ &+ (q_x + q_y)\Gamma_3 + (q_x - q_y)\Gamma_4 \\ &+ \frac{1}{\sqrt{3}}(2q_z - q_x - q_y)\Gamma_5\Big],\end{aligned} \tag{A22}$$

up to the first order of $\vec{q} = (q_x, q_y, q_z)$. In addition, we apply the second-order degenerate perturbation theory on the magnetic field Hamiltonian [Eq. (A9)]. We denote $\gamma_1 = B\cos\theta$ and $\gamma_2 = B\sin\theta$. Concentrating on two crossing bands, we obtain the following effective model,

$$\mathcal{H}^{001}_{\mathrm{proj},C1} = A_0\sigma_0 + A_1\sigma_x + A_2\sigma_y + A_3\sigma_z, \tag{A23}$$

where

$$\begin{aligned}A_0 &= \frac{\sqrt{3}}{6}\gamma_1 + \frac{13\sqrt{3}}{24}\gamma_2, \\ A_1 &= -\sqrt{\frac{\alpha}{6}}[-(2-\sqrt{3})q_x - (2+\sqrt{3})q_y - 2q_z] \\ &\quad - \frac{\gamma_1^2}{4\sqrt{2}\alpha} - \frac{9\gamma_2^2}{64\sqrt{2}\alpha}, \\ A_2 &= -\sqrt{\frac{\alpha}{6}}[(2+\sqrt{3})q_x + (2-\sqrt{3})q_y + 2q_z] \\ &\quad + \frac{\gamma_1^2}{4\sqrt{2}\alpha} + \frac{9\gamma_2^2}{64\sqrt{2}\alpha}, \\ A_3 &= \sqrt{\frac{\alpha}{3}}(q_x + q_y - 2q_z) + \frac{\sqrt{3}\gamma_1}{3} + \frac{7\sqrt{3}\gamma_2}{120}.\end{aligned}$$

Weyl points will exist when $A_1 = A_2 = A_3 = 0$. The solutions are

$$\begin{aligned}q_x = q_y &= \frac{-16\alpha(4\gamma_1 + 7\gamma_2) + \sqrt{3}\left(16\gamma_1^2 + 9\gamma_2^2\right)}{384\alpha^{3/2}}, \\ q_z &= \frac{32\alpha(4\gamma_1 + 7\gamma_2) + \sqrt{3}\left(16\gamma_1^2 + 9\gamma_2^2\right)}{384\alpha^{3/2}}.\end{aligned} \tag{A24}$$

The rotation symmetry $C_{2z}$ and inversion $P$ determine the trajectory of the other 3 class 1 Weyl points.

Meanwhile, at one of the class 2 Weyl points $\vec{k}_{C2,001} = \sqrt{\frac{\alpha}{3}}(-1, 1, 1)$, the Hamiltonian at $\vec{k} = \vec{k}_{C2,001} + \vec{q}$ is

$$\mathcal{H}^{001}_{C2} = \mathcal{H}^{001}_{0,C2} + \mathcal{H}^{001}_{\mathrm{mom},C2}, \tag{A25}$$

where

$$\mathcal{H}^{001}_{0,C2} = \frac{\alpha}{\sqrt{3}}[-\Gamma_1 + \Gamma_2 + \Gamma_3] - \alpha\Gamma_{45}, \tag{A26}$$

$$\begin{aligned}\mathcal{H}^{001}_{\mathrm{mom},C2} = &-\sqrt{\alpha}\Big[(q_y + q_z)\Gamma_1 + (q_x - q_z)\Gamma_2 \\ &+ (q_x - q_y)\Gamma_3 - (q_x + q_y)\Gamma_4 \\ &+ \frac{1}{\sqrt{3}}(2q_z + q_x - q_y)\Gamma_5\Big],\end{aligned} \tag{A27}$$

up to the first order of $\vec{q}$. By the same procedure as for class 1, we obtain the following Hamiltonian,

$$\mathcal{H}^{001}_{\mathrm{proj},C2} = B_0\sigma_0 + B_1\sigma_x + B_2\sigma_y + B_3\sigma_3, \tag{A28}$$

where

$$\begin{aligned}B_0 &= -\frac{\sqrt{3}\gamma_1}{6} - \frac{13\sqrt{3}\gamma_2}{24}, \\ B_1 &= -\sqrt{\frac{\alpha}{6}}[-(2+\sqrt{3})q_x + (2-\sqrt{3})q_y + 2q_z] \\ &\quad + \left(\frac{\gamma_1^2}{\alpha}\frac{1}{4\sqrt{2}} + \frac{\gamma_2^2}{\alpha}\frac{9}{64\sqrt{2}}\right), \\ B_2 &= -\sqrt{\frac{\alpha}{6}}[-(2-\sqrt{3})q_x + (2+\sqrt{3})q_y + 2q_z] \\ &\quad + \left(\frac{\gamma_1^2}{\alpha}\frac{1}{4\sqrt{2}} + \frac{\gamma_2^2}{\alpha}\frac{9}{64\sqrt{2}}\right), \\ B_3 &= -\sqrt{\frac{\alpha}{3}}(q_x - q_y + 2q_z) - \left(\gamma_1\frac{\sqrt{3}}{3} + \gamma_2\frac{7\sqrt{3}}{12}\right).\end{aligned}$$

Therefore, the Weyl points are at

$$\begin{aligned}q_x = -q_y &= -\frac{16\alpha(4\gamma_1 + 7\gamma_2) + \sqrt{3}\left(16\gamma_1^2 + 9\gamma_2^2\right)}{384\alpha^{3/2}}, \\ q_z &= \frac{-32\alpha(4\gamma_1 + 7\gamma_2) + \sqrt{3}\left(16\gamma_1^2 + 9\gamma_2^2\right)}{384a^{3/2}}.\end{aligned} \tag{A29}$$

The other 3 class 2 Weyl points are determined by threefold rotation and inversion symmetry. The result implies that Weyl points can only move on the mirror plane [1$\bar{1}$0] or [110], and the direction of the trajectory of each class is distinct. The trajectories are drawn in Fig. 10.

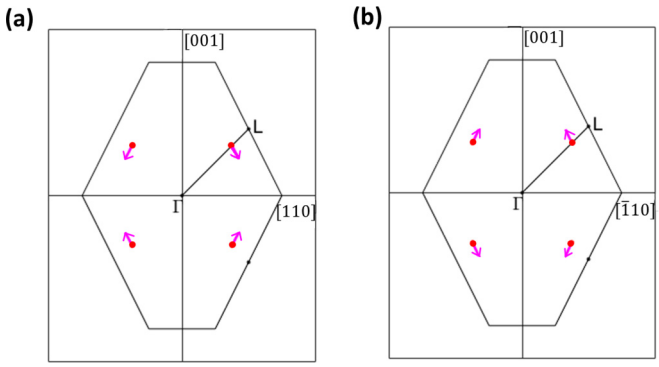


FIG. 10. (a) Under the [001] magnetic field, the trajectories of class 1 Weyl points on the mirror $[1\bar{1}0]$ plane and (b) class 2 Weyl points are drawn on the mirror [110] plane with colored lines ($\gamma_1 = \gamma_2$). The black solid line is a virtual boundary of the Brillouin zone to present the trajectories of Weyl points in an obvious way.

From now on, we introduce two variables $\theta$ and $\phi$. The effective theory at the $\Gamma$ point with AIAO order and the [001] magnetic field is

$$\begin{aligned}\mathcal{H}_\Gamma &= \mathcal{H}_{\mathrm{AIAO}} + \mathcal{H}_{B,001} \\ &= -\alpha\left(\Gamma_{45} + \tan\phi\cos\theta J_z + \tan\phi\sin\theta J_z^3\right). \quad \text{(A30)}\end{aligned}$$

We observe crossing points through perturbation near the $\Gamma$ point and projection onto two bands. To complement the argument, we use the numerical method to observe crossing points throughout $k$ space. We introduce a pedagogical scheme to observe the crossing points.

If we let $\gamma = \tan\phi$ and $\theta = \frac{2\pi}{3}$, then $\gamma$ is the only variable. The energy eigenvalues at $\Gamma$ are

$$E_\pm^1 = \tfrac{1}{16}[(4-13\sqrt{3})\gamma \pm 2\sqrt{64+(163-53\sqrt{3})\gamma^2}],$$

$$E_\pm^2 = \tfrac{1}{16}[(13\sqrt{3}-4)\gamma \pm 2\sqrt{64+(163-53\sqrt{3})\gamma^2}].$$

$J_z = \pm 3/2, \pm 1/2$ are not eigenstates of this Hamiltonian anymore. Since $E_+^1$ and $E_-^2$ are degenerate when $\gamma^* \approx 1.8019$, the energy level sequence changes from $E_-^1 < E_+^1 < E_-^2 < E_+^2$ to $E_-^1 < E_-^2 < E_+^1 < E_+^2$ as $\gamma$ increases. In fact, the sequence exchange between $E_+^1$ and $E_-^2$ at $\gamma^*$ causes the change of the nature of the crossing points of the two middle bands.

We consider the Luttinger Hamiltonian [Eq. (1)] as a perturbation to describe the crossing near $\Gamma$. Then, we project the perturbation Hamiltonian onto any pair of bands. We can establish 6 possible choices, and observe whether the bands cross or not. Here, we denote $E_1(\vec{k})$ to be $E_-^1$, $E_2(\vec{k})$ to be $E_-^2$, $E_3(\vec{k})$ to be $E_+^1$, $E_4(\vec{k})$ to be $E_+^2$, at the $\Gamma$ point. Only four choices have crossing points: $E_1$ and $E_2$, $E_1$ and $E_3$, $E_2$ and $E_4$, and $E_3$ and $E_4$, and other choices are gapped.

The projected Hamiltonian has a form like

$$H_{\mathrm{proj},\Gamma} = G_0\sigma_0 + G_1\sigma_1 + G_2\sigma_2 + G_3\sigma_3, \quad \text{(A31)}$$

and crossing points are at the solution of $G_1 = G_2 = G_3 = 0$. For example, for $E_1$ and $E_2$, one may obtain a system of equations

$$\begin{aligned}&\text{(i) } k_x k_z = 0,\\ &\text{(ii) } k_y k_z = 0,\\ &\text{(iii) } 128\sqrt{3}k_x k_y + \gamma[8(-4+7\sqrt{3})(k_x^2+k_y^2-2k_z^2)\\ &\quad + (4-13\sqrt{3})\eta_1] = 0,\end{aligned}$$

where $\eta_1 = \sqrt{64+(163-56\sqrt{3})\gamma^2}$. The solutions are

$$\text{(i) } k_x = \pm\sqrt{\frac{257}{1048}+\frac{3\sqrt{3}}{131}}\eta_1^{1/2}, \quad k_y = 0, k_z = 0,$$

$$\text{(ii) } k_y = \pm\sqrt{\frac{257}{1048}+\frac{3\sqrt{3}}{131}}\eta_1^{1/2}, \quad k_x = 0, k_z = 0,$$

$$\begin{aligned}&\text{(iii) } 128\sqrt{3}k_x k_y + \gamma\left[8(-4+7\sqrt{3})(k_x^2+k_y^2)\right]\\ &\quad = \gamma(-4+13\sqrt{3})\eta_1.\end{aligned}$$

The solutions (i) and (ii) are, in fact, consistent with the $k_x$ and $k_y$ intersection of (iii), which forms a line node on the $k_z = 0$ plane. The line node changes its shape as varying $\gamma$: it is hyperbolic if $\gamma < 1.7055$, a line if $\gamma = 1.7055$, and an ellipse if $\gamma > 1.7055$.

One can obtain the solutions for other choices with the same way. To sum up, we can classify the solutions into 5 groups:

(1) The crossing between $E_1$ and $E_2$, at energy $E^* = -\frac{1}{8}\eta_1$, whose form is a line node on the $k_z = 0$ plane; the line node changes from a hyperbola to a line and to an ellipse as $\gamma$ increases.

(2) The crossing between $E_1$ and $E_3$, at energy $E^{**} = -\frac{1}{16}\eta_2$, whose form is 2 pairs of Weyl points on the $[1\bar{1}0]$ plane, existing only for $\gamma < 0.5685$.

(3) The crossing between $E_2$ and $E_4$, at energy $E^{***} = \frac{1}{16}\eta_2$, whose form is 2 pairs of Weyl points on the [110] plane, existing for every $\gamma$.

(4) The crossing between $E_3$ and $E_4$, at energy $E^{****} = \frac{1}{8}\eta_1$, whose form is a hyperbola on the $k_z = 0$ plane, only existing for $\gamma < 1.7055$.

(5) The crossing between $E_3$ and $E_4$, at energy $E^{****} = \frac{1}{8}\eta_1$, whose form is a pair of Weyl points at the $k_z$ axis, existing for every $\gamma$.

For all of these, $\eta_2 = (13\sqrt{3}-4)\gamma$.

Although there are various crossings, we concentrate on the crossings between two middle bands repeatedly. Accordingly, we construct a phase diagram by such crossings. In Fig. 11, a 4-pair Weyl semimetal (4P WSM), a type-1 2-pair Weyl semimetal (T1-2P WSM), and a line-node semimetal (LSM) emerge. The T1-2P WSM denotes the phase in which group 2 Weyl points in the $[1\bar{1}0]$ plane are annihilated while group 3 Weyl points in the [110] plane remain. Remarkably, the phase transition from 4P WSM to 2P WSM is attributed to the annihilation of Weyl points, but the transition from 2P WSM to LSM comes from the energy level sequence exchange between crossing points.

Applying the approach to various $\theta$ and $\gamma = \tan\phi$, we acquire a 2D phase diagram in Fig. 6. In the phase diagram, in addition to 4P WSM, T1-2P WSM, and LSM, a type-2 2-pair

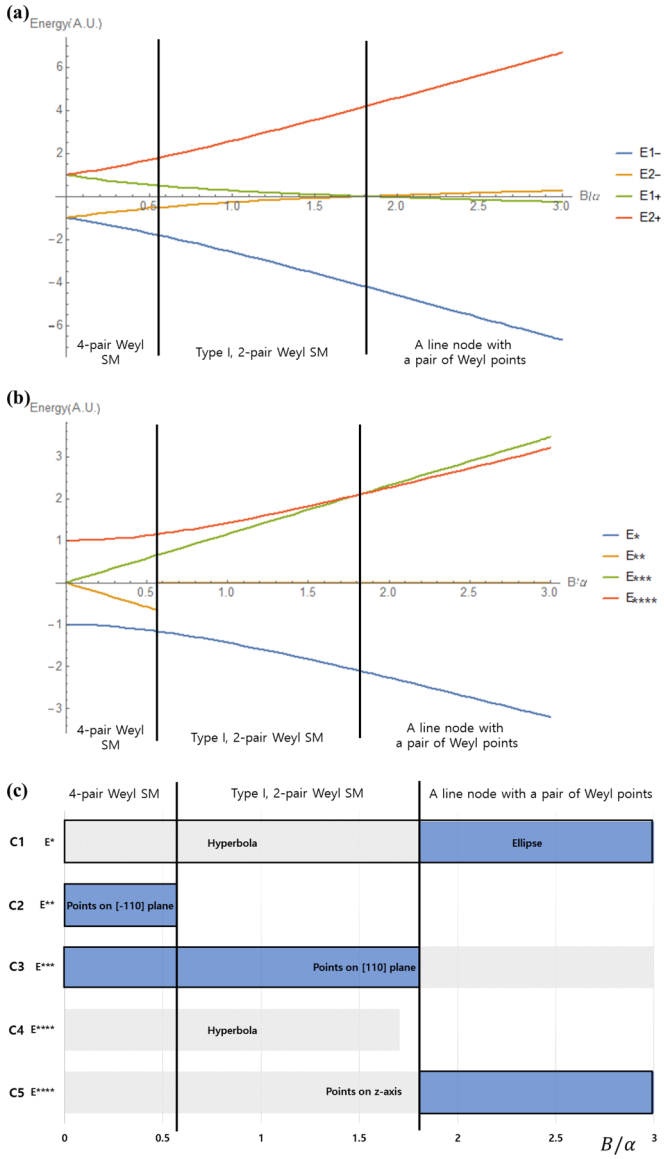


FIG. 11. (a) Energy spectra at the Γ point is drawn by changing $\gamma$. (b) The crossing energy is drawn by changing $\gamma$. We assume the angular momentum unit to be 1, and apply the unit effective Zeeman field. (c) A schematic diagram of 5 classes of crossings is shown against $\gamma$. Each solution class can exist in the blue- and gray-shaded regions. The meaning of blue-shaded regions is the crossing between two middle bands. For both figures, the phase diagrams are represented together.

Weyl semimetal (T2-2P WSM) and a double Weyl semimetal (DWSM) emerge. T2-2P WSM is the phase in which group 2 points remain while group 3 points vanish. The phase transition from 2P WSM to DWSM emerges from merging a pair of Weyl points with the same topological charge at the $k_z$ axis.

In summary, the result implies that diverse topological phases can arise by changing $\theta$ and $\phi$, and which phase transition occurs depends heavily on the interplay between the Zeeman and Luttinger $q$ term. It turns out that for a certain range of $\theta$ ($\theta_{b1} < \theta < \theta_{b2}, \theta_{b3} < \theta < \theta_{b4}$), LSM appears, while DWSM emerges for the remaining range. For DWSM and LSM, not only are the shape and positions of crossings different, but also the ways of the phase transition are disparate. The phase transition from 2P WSM to DWSM occurs by the combination of Weyl points at the high-symmetry line, while the transition from 2P WSM to LSM is from when the exchange of energy level sequence at the Γ point changes two middle bands.

### *b. [111] direction*

Under the [111] direction field, we begin to study the trajectories of 8 Weyl points under a large AIAO order parameter and small magnetic field. Since threefold rotation around the [111] line $C_{3,111}$ is still preserved, 8 Weyl points will be divided into 2 classes again. Class 1 includes 2 Weyl points along the [111] line, while class 2 includes the other 6 Weyl points. Class 1 points will never deviate from the [111] line, and class 2 points will travel only on the mirror planes, according to the symmetries and the topological nature of Weyl points.

For class 1, let us choose $\vec{k}_{C1,111} = \sqrt{\frac{\alpha}{3}}(1,1,1)$. The Hamiltonian near the Weyl points is just

$$\mathcal{H}^{111}_{C1} = \mathcal{H}^{001}_{C1}, \tag{A32}$$

while the magnetic field Hamiltonian is Eq. (A19).

After the same procedure as the analysis for the [001] direction, we have

$$\mathcal{H}^{111}_{\text{proj},C1} = A_0\sigma_0 + A_1\sigma_x + A_2\sigma_y + A_3\sigma_z, \tag{A33}$$

where

$$\begin{aligned} A_0 &= \frac{\sqrt{3}}{2}\beta_1 + \frac{3}{2}\frac{\beta_1^2}{\alpha} + \frac{13\sqrt{3}}{8}m_2 + \frac{147}{32}\frac{m_2^2}{\alpha}, \\ A_1 &= -\frac{3}{2\sqrt{2}}\frac{\beta_1^2}{\alpha} - \frac{147}{32\sqrt{2}}\frac{\beta_2^2}{\alpha} \\ &\quad -\sqrt{\alpha}\left[\frac{-(2-\sqrt{3})q_x - (2+\sqrt{3})q_y - 2q_z}{\sqrt{6}}\right], \\ A_2 &= \frac{3}{2\sqrt{2}}\frac{\beta_1^2}{\alpha} + \frac{147}{32\sqrt{2}}\frac{\beta_2^2}{\alpha} \\ &\quad -\sqrt{\alpha}\left[\frac{(2+\sqrt{3})q_x + (2-\sqrt{3})q_y + 2q_z}{\sqrt{6}}\right], \\ A_3 &= \frac{\sqrt{\alpha}(q_x + q_y - 2q_z)}{\sqrt{3}}. \end{aligned} \tag{A34}$$

Weyl points exist at the solutions of $A_1 = A_2 = A_3 = 0$,

$$(q_x, q_y, q_z) = \frac{\sqrt{3}}{64}\frac{16\beta_1^2 + 49\beta_2^2}{\alpha^{3/2}}(1,1,1). \tag{A35}$$

According to the inversion symmetry, another Weyl point in class 1 moves to $(q_x, q_y, q_z) = -\frac{\sqrt{3}}{64}\frac{16\beta_1^2+49\beta_2^2}{\alpha^{3/2}}(1,1,1)$. Class 1 Weyl points stick on the [111] line.

On the other hand, if we choose one of the class 2 Weyl points, $\vec{k}_{C2,111} = \sqrt{\frac{\alpha}{3}}(1,1,-1)$, the Hamiltonian is

$$\mathcal{H}^{111}_{C2} = \mathcal{H}^{111}_{0,C2} + \mathcal{H}^{111}_{\text{mom},C2}, \tag{A36}$$

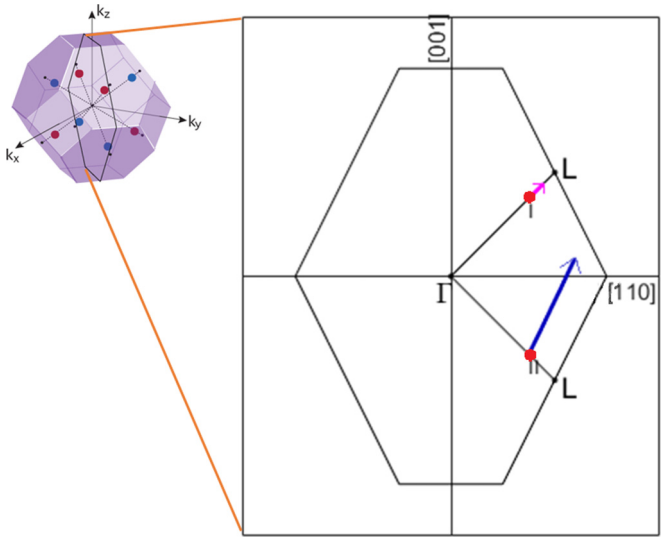


FIG. 12. Under the [111] effective field, the trajectories of Weyl points are drawn in colored lines when the Zeeman and Luttinger $q$ term are equally contributed ($\beta_1 = \beta_2$). The class 1 Weyl point in a pink line never deviates from the [111] axis, while the class 2 Weyl point in a blue line moves away from the symmetry line, but still remains on the mirror plane. There is no zone boundary in this model, yet it is drawn in order to visualize the Weyl points effectively.

where

$$\begin{aligned}\mathcal{H}^{111}_{0,C2} &= \frac{\alpha}{\sqrt{3}}(\Gamma_1+\Gamma_2-\Gamma_3)-\alpha\Gamma_{45},\\ \mathcal{H}^{111}_{\mathrm{mom},C2} &= -\sqrt{\alpha}[(q_z-q_y)\Gamma_1+(q_z-q_x)\Gamma_2\\ &\quad+(q_x+q_y)\Gamma_3+(q_x-q_y)\Gamma_4\\ &\quad+\frac{1}{\sqrt{3}}(-2q_z-q_x-q_y)\Gamma_5], \end{aligned} \tag{A37}$$

up to first order of $\vec{q} = \vec{k} - \vec{k}_{C2,111}$. The magnetic field Hamiltonian is Eq. (A19), again.

Given by the same procedure, the class 2 Weyl point will be at

$$\begin{aligned} q_x = q_y &= \frac{-16\alpha(4\beta_1+7\beta_2)+\sqrt{3}\left(48\beta_1^2+151\beta_2^2\right)}{192\alpha^{3/2}},\\ q_z &= \frac{-32\alpha(4\beta_1+7\beta_2)+\sqrt{3}\left(48\beta_1^2+395\beta_2^2\right)}{192\alpha^{3/2}}. \end{aligned} \tag{A38}$$

For the other 5 Weyl points, $C_{3,111}$ and $P$ determine the trajectories. Class 2 Weyl points deviate away from the high-symmetry axes due to the threefold rotational symmetry breaking, but the points cannot travel out of the mirror planes by $\sigma_{d,111}T$ symmetries. If class 2 Weyl points move out of the plane, the Nielsen-Ninomiya theorem is violated. The trajectories of both classes of Weyl points are drawn in Fig. 12.

Next, we investigate the crossing point by varying $\theta$ and $\phi$. The Hamiltonian is

$$\mathcal{H} = \mathcal{H}_0 + \mathcal{H}_{\mathrm{AIAO}} + \mathcal{H}_{B,111}. \tag{A39}$$

According to the previous section, double Weyl points emerge only if $J_{[111]} = \pm 3/2$ are eigenstates of the Hamiltonian.

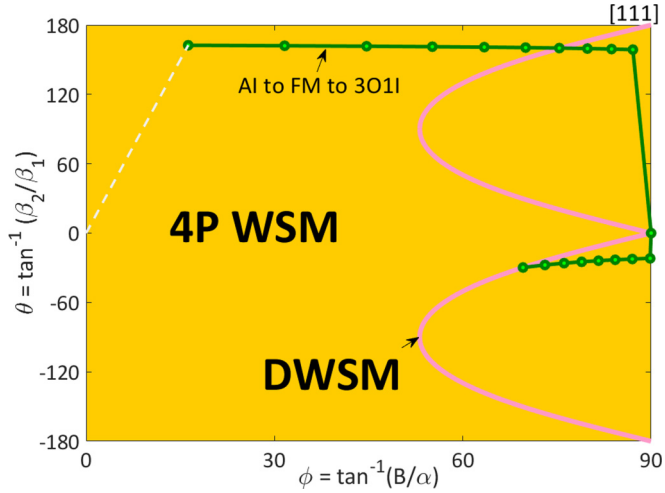


FIG. 13. A general 2D phase diagram under the [111] direction effective field is drawn. A couple of topological phases, the 4-pair Weyl semimetal (4P WSM) and double Weyl semimetal (DWSM), can be observed. The green line shows the projection of the Hubbard interaction, from AI to FM to 3O1I.

Finding the condition that $J_{[111]}$ eigenstates diagonalize the Hamiltonian $H$, one can obtain a line for the DWSM phase. In Fig. 13, we represent a general phase diagram under the [111] direction of the effective field.

In a nutshell, we observe a number of distinct topological phases under the effective field: DWSM, 4P WSM, T1/T2-2P WSM, and LSM. The interplay between diverse magnetic terms plays an important role in the emergence of distinct topological phases.

## APPENDIX B: EFFECTIVE THEORY AT THE $L$ POINT

According to previous research [12], if the AIAO order parameter is developed, pyrochlore iridates become the insulating phase. In order to observe topological phases near the insulating phase, we should study the effective theory near the $L$ point. $L$ points have lower symmetry than the $\Gamma$ point; only $T$, $P$, $C_3$, and some of $\sigma_d$ are preserved.

### 1. General Hamiltonian at the $L$ point

By the inversion symmetry $P$ at the $L$ point, energy eigenstates at the $L$ point must have either one of $P$ eigenvalues, $\pm 1$ ($P^2 = 1$). We choose two eigenstates with distinct eigenvalues. If we take $P = \sigma_z$, the 2-band Hamiltonian at the $L$ point will be

$$\mathcal{H}_L = \Delta\sigma_z. \tag{B1}$$

Let us define the local $z$ direction to be along the threefold rotation axis, and the local $y$ direction be in the mirror plane. Near the $L$ point, the most general Hamiltonian which is invariant under $P$ symmetry up to the second order of momentum $\vec{q} = \vec{k} - \vec{k}_L$ is

$$\mathcal{H}_1(\vec{q}) = A_1(\vec{q})\sigma_x + B_1(\vec{q})\sigma_y + [C_1(\vec{q}) + D_1(\vec{q})]\sigma_z, \tag{B2}$$

such that

$$A_1(\vec{q}) = a_1 q_x + a_2 q_y + a_3 q_z,$$
$$B_1(\vec{q}) = b_1 q_x + b_2 q_y + b_3 q_z,$$
$$C_1(\vec{q}) = \Delta + \frac{q_x^2}{2m_x} + \frac{q_y^2}{2m_y} + \frac{q_z^2}{2m_z},$$
$$D_1(\vec{q}) = c_1 q_x q_y + c_2 q_x q_z + c_3 q_y q_z.$$

Next, we impose $\sigma_d T$ symmetry upon this Hamiltonian. Considering that $\sigma_d T$ is antiunitary, $(\sigma_d T)^2 = 1$, and $\Delta\sigma_z$ is invariant under the symmetry, one can choose $\sigma_d T = K$ (complex conjugate). The general Hamiltonian near the $L$ point under $P$ and $\sigma_d T$ is

$$\mathcal{H}_2(\vec{q}) = A_2(\vec{q})\sigma_x + B_2(\vec{q})\sigma_y + [C_2(\vec{q}) + D_2(\vec{q})]\sigma_z, \quad \text{(B3)}$$

where

$$A_2(\vec{q}) = a_1 q_x,$$
$$B_2(\vec{q}) = b_2 q_y + b_3 q_z,$$
$$C_2(\vec{q}) = \Delta + \frac{q_x^2}{2m_x} + \frac{q_y^2}{2m_y} + \frac{q_z^2}{2m_z},$$
$$D_2(\vec{q}) = c_3 q_y q_z.$$

Finally, we add up threefold rotation symmetry about the local $z$ axis, $C_3 = e^{i\frac{2\pi}{3}\sigma_z}$. The general Hamiltonian under the $L$ point under $P$, $\sigma_d T$, and $C_3$ is

$$\mathcal{H}_3(\vec{q}) = a(q_x\sigma_x + q_y\sigma_y) + \left(\Delta + \frac{q_x^2 + q_y^2}{2m_{xy}} + \frac{q_z^2}{2m_z}\right)\sigma_z. \quad \text{(B4)}$$

$\mathcal{H}_2$ is the most general Hamiltonian with $P$ and $\sigma_d T$, while $\mathcal{H}_3$ is the most general Hamiltonian with $P$, $\sigma_d T$, and $C_3$.

We can establish the general Hamiltonian with the effective field up to first order under $P$ and $\sigma_d T$, as well:

$$\mathcal{H}_{2B}(\vec{q}, \vec{B}) = A_{2B}\sigma_x + B_{2B}\sigma_y + C_{2B}\sigma_z, \quad \text{(B5)}$$

where

$$A_{2B} = q_x(d_1 B_y + d_2 B_z) + B_x(d_3 q_y + d_4 q_z),$$
$$B_{2B} = B_y(e_1 q_y + e_2 q_z) + B_z(e_3 q_y + e_4 q_z),$$
$$C_{2B} = f_1 B_y + f_2 B_z.$$

Adding $C_3$ symmetry, one can find the Hamiltonian with magnetic field:

$$\mathcal{H}_{3B}(\vec{q}, \vec{B}) = gB_z(q_x\sigma_x + q_y\sigma_y) + f_2 B_z\sigma_z. \quad \text{(B6)}$$

### 2. [111] direction

Here, we begin with the phase of the [111] direction of the effective field since we can understand the phase of the [001] direction through the argument in this section.

We divide all of the 4 $L$ points in the Brillouin zone into 2 classes: the class 1 $L$ point is an $L$ point on the [111] axis, while class 2 $L$ points are the other three. Without magnetic field, the Hamiltonian is just Eq. (B4) for every $L$ point. We obtain the position of the Weyl point as

$$q_x = q_y = 0, \quad q_z = \pm\sqrt{-2m_z\Delta}.$$

A pair of Weyl points exist along the local $z$ axis only if $m_z\Delta < 0$.

If we apply the magnetic field on the system, every symmetry of the class 1 $L$ point remains preserved,

$$\mathcal{H}_{111}^{L,C1} = \mathcal{H}_3 + \mathcal{H}_{3B} = a'(q_x\sigma_x + q_y\sigma_y) + \left(\Delta' + \frac{q_x^2 + q_y^2}{2m_{xy}} + \frac{q_z^2}{2m_z}\right)\sigma_z, \quad \text{(B7)}$$

where

$$a' = a + gB_z, \ \Delta' = \Delta + f_2 B_z.$$

Since the form of Eq. (B7) is the same as Eq. (B4), the positions of the Weyl points are just $(q_x, q_y, q_z) = (0, 0, \pm\sqrt{-2m_z\Delta'})$. That is, Weyl points can only move along the local $z$ axis, which corresponds to the global [111] line. Furthermore, if $-m_z\Delta' = 0$, two Weyl points meet at the origin, and if $-m_z\Delta' > 0$, the pair of Weyl points are annihilated. If $m_z > 0$, then the condition for the gapless state is $\Delta' = \Delta + f_2 B_z < 0$.

At class 2 $L$ points, $C_3$ symmetry is broken:

$$\mathcal{H}_{111}^{L,C2} = \mathcal{H}_2 + \mathcal{H}_{2B} = A_2'(\vec{q})\sigma_x + B_2'(\vec{q})\sigma_y + [C_2'(\vec{q}) + D_2'(\vec{q})]\sigma_z, \quad \text{(B8)}$$

where

$$A_2(\vec{q}) = q_x(a_1 + d_1 B_y + d_2 B_z) = a_1' q_x,$$
$$B_2(\vec{q}) = q_y(b_2 + e_1 B_y + e_3 B_z) + q_z(b_3 + e_2 B_y + e_4 B_z) = b_2' q_y + b_3' q_z,$$
$$C_2(\vec{q}) = (\Delta + f_1 B_y + f_2 B_z) + \frac{q_x^2}{2m_x} + \frac{q_y^2}{2m_y} + \frac{q_z^2}{2m_z} = \Delta'' + \frac{q_x^2}{2m_x} + \frac{q_y^2}{2m_y} + \frac{q_z^2}{2m_z},$$
$$D_2(\vec{q}) = c_3 q_y q_z. \quad \text{(B9)}$$

Note that $B_x = 0$ here, since the magnetic field direction is in the $k_x = 0$ plane for class 2 $L$ points. Without magnetic field, we should obtain $H_{3B}$ again, so that $b_2 = a_1$, $b_3 = c_3 = 0$, and $m_x = m_y = m_{xy}$. The Hamiltonian Eq. (B8) is just the renormalization of some variables in Eq. (B3). Weyl points will exist at

$$q_x = 0, \quad q_y = \pm\frac{b_3'}{b_2'}\sqrt{-\Delta''\left(\frac{b_3'^2}{2m_{xy}b_2'^2} + \frac{1}{2m_z}\right)},$$
$$q_z = \pm\sqrt{-\Delta''\left(\frac{b_3'^2}{2m_{xy}b_2'^2} + \frac{1}{2m_z}\right)}.$$

A pair of Weyl points exists only if $-\Delta''(\frac{b_3'^2}{2m_{xy}b_2'^2} + \frac{1}{2m_z}) \equiv -\Delta'' X > 0$, and the pair annihilation occurs at the origin if $\Delta'' = 0$. If we assume $X > 0$, Weyl points exist when $\Delta'' < 0$. Near class 2 $L$ points, Weyl points can move off from the high-symmetry line and travel through the local $yz$ mirror plane. The result is consistent with the trajectory in the $\Gamma$ effective theory of Appendix A 5 b.

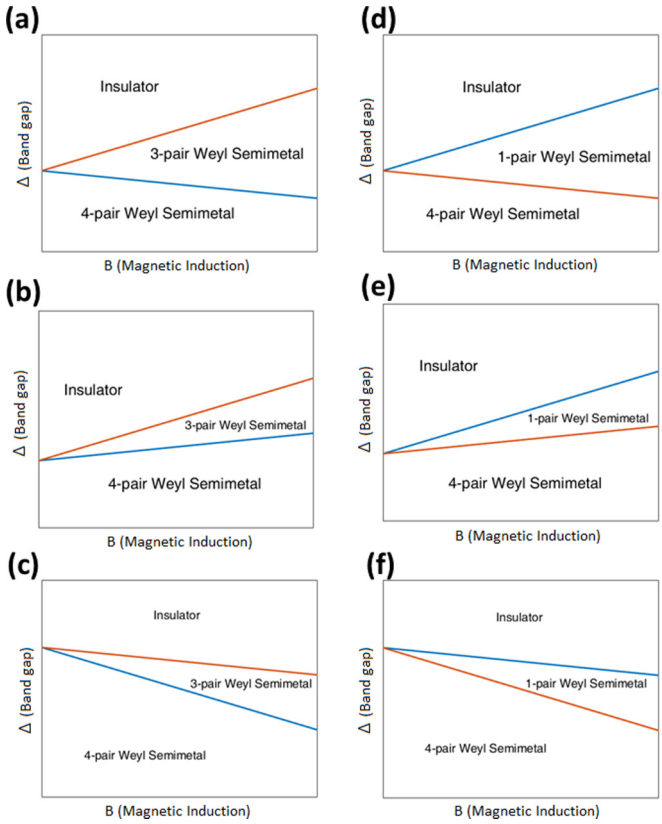


FIG. 14. The possible phase diagrams near the insulating phase of pyrochlore iridates under the [111] direction of the effective field are shown. The blue lines are where the class 1 $L$ points become gapless, while the orange lines are where the class 2 $L$ points become gapless. The slope of each line is (a) $f_2 = 0.1$, $f_2' = -0.3$, (b) $f_2 = -0.3$, $f_2' = 0.1$, (c) $f_2 = -0.1$, $f_2' = -0.3$, (d) $f_2 = -0.3$, $f_2' = -0.1$, (e) $f_2 = 0.3$, $f_2' = 0.1$, and (f) $f_2 = 0.1$, $f_2' = 0.3$.

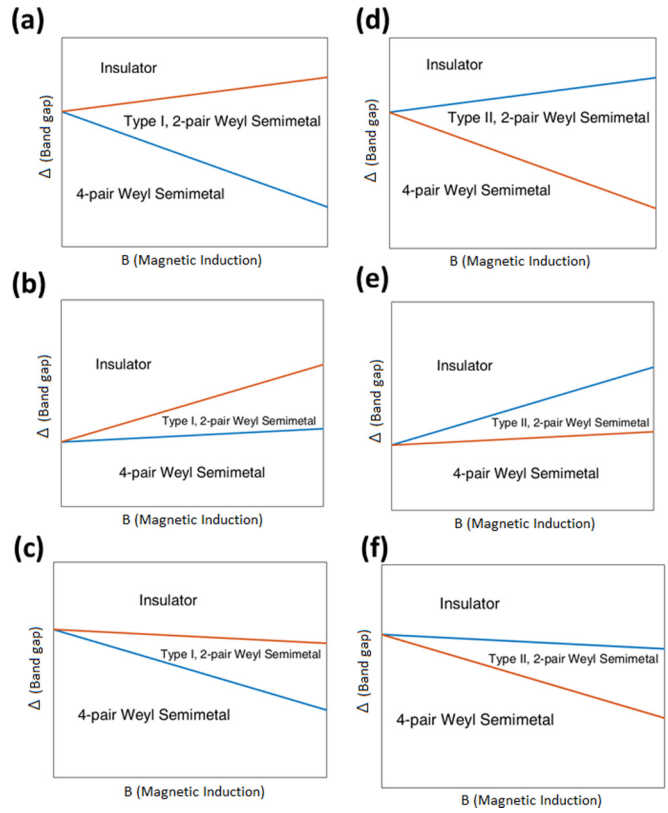


FIG. 15. The possible phase diagrams near the Weyl semimetal–insulating phase transition under the [001] direction field are shown. The blue lines are where the class 1 $L$ points become gapless, while the orange lines are where the class 2 $L$ points become gapless. The slope of each line is (a) $f_1' = 0.2$, $f_2' = 0.2$, (b) $f_1' = 0.1$, $f_2' = -0.3$, (c) $f_1' = 0.1$, $f_2' = 0.3$, (d) $f_1' = -0.2$, $f_2' = 0.2$, (e) $f_1' = -0.1$, $f_2' = -0.3$, (f) $f_1' = -0.1$, $f_2' = 0.3$.

In summary, we have two equations to obtain phase transitions:

$$\Delta + f_2 B = 0, \quad \Delta + f_2' B = 0.$$

Usually, $f_2$ and $f_2'$ do not have to be equal to each other. In Fig. 14, we represent all possible forms of the phase diagram by changing $f_2$ and $f_2'$. One can observe a 4-pair Weyl semimetal (4P WSM), 3-pair Weyl semimetal (3P WSM), 1-pair Weyl semimetal (1P WSM), and trivial insulator (INS). Which topological semimetal emerges depends on the sequence of Weyl point annihilation. If Weyl points are annihilated at the class 1 $L$ point first, we can observe the 3-pair Weyl semimetal, while if Weyl points are annihilated at the class 2 $L$ point first, we can observe the 1-pair Weyl semimetal.

### 3. [001] direction

Under the [001] direction of the effective field, we divide 4 $L$ points into 2 classes again: a pair of $L$ points in the $[1\bar{1}0]$ plane are class 1, and another pair of $L$ points in the [110] plane are class 2. Since threefold rotational symmetries are broken while $2\sigma_d T$ remains, both classes are just the same as the class 2 Weyl points of the [111] case. Again, we set the local $z$ axis along the threefold rotation axis, and the local $y$ axis inside the mirror plane. Recalling Eq. (B8) and the solutions, we confront the two following equations as well:

$$\Delta + f_1' B = 0, \quad \Delta + f_2' B = 0.$$

By controlling $f_1'$ and $f_2'$, we draw several forms of phase diagrams in Fig. 15.

In the phase diagram, we observe type I and II 2-pair Weyl semimetals. T1-2P WSM denotes the semimetal without Weyl points near the class 1 $L$ points, while T2-2P WSM denotes that without Weyl points near the class 2 $L$ points. The sequence of Weyl point annihilation determines the topological semimetallic phase. If class 1/2 Weyl points are annihilated initially, then the T1/2-2P WSM appears.

In summary, we can observe the emergent topological phases such as 3P WSM, T1/2-2P WSM, and 1P WSM near the insulating phase.

## APPENDIX C: CLUSTER MAGNETIC MULTIPOLE IN PYROCHLORE IRIDATES

### 1. Cluster magnetic multipoles

Suppose we have a piece of magnetic matter localized in real space. Then, the Ampere-Maxwell law becomes

$$\nabla^2 \vec{A} = \mu_0 \vec{J} \tag{C1}$$

outside the matter, under Coulomb gauge ($\nabla \cdot \vec{A} = 0$). By Green's theorem, we obtain the general solution as

$$\vec{A} = \sum_{p=0}^{\infty} \sum_{q=-p}^{p} \frac{1}{r^{p+1}} \vec{Z}_{pq}(\theta, \phi) M_{pq}, \tag{C2}$$

where

$$\vec{Z}_{pq} = -\frac{i}{p} \vec{L} \left[ \sqrt{\frac{4\pi}{2p+1}} Y_{pq}(\theta, \phi) \right],$$

$$M_{pq} = \sqrt{\frac{4\pi}{2p+1}} \int d^3 r' \, \nabla' [r'^p Y^*_{pq}(\theta', \phi')] \cdot \vec{M}(\vec{r}'), \tag{C3}$$

such that $\vec{L}$ is angular momentum, $Y_{pq}(\theta, \phi)$ is spherical harmonics, and $\vec{M}(\vec{r}')$ is the magnetization density defined by $\vec{J}(\vec{r}') = c \nabla \vec{M}(\vec{r}')$. This process is called multipole expansion, and $M_{pq}$ is called the magnetic multipole. In general, we can express any configuration of magnetic matter in a series of multipoles [28].

Applying the same argument in the lattice, we can define the cluster magnetic multipole moment (CMMM) [27]. An atom cluster is defined as a group of atoms connected by point group operators within a magnetic unit cell. The CMMM at the $a$th cluster in the magnetic unit cell is simply defined the same as in Eq. (C3),

$$M^a_{pq} = \sqrt{\frac{4\pi}{2p+1}} \sum_{i=1}^{N_a} \nabla \left[ r_i^p Y^*_{pq}(\theta_i, \phi_i) \right] \cdot \vec{m}_i, \tag{C4}$$

where $\vec{m}_i$ is the magnetic moment at the $i$th site, and $N_a$ is the number of atoms in the $a$th cluster. This is a spherical tensor of rank $p$. If $p = 1, 2$, and 3, then we can acquire the dipoles, quadrupoles, and octupoles of the cluster, respectively. The contribution of the magnetic unit cell to the CMMM is just the summation over every cluster in the cell,

$$M_{pq} = \frac{N^u}{N^c} \frac{1}{V} \sum_{a=1}^{N} M^a_{pq}, \tag{C5}$$

where $N^u$ is the number of atoms of the magnetic unit cell, $N^c$ is the total number of atoms in every cluster, $N$ is the number of clusters, and $V$ is the volume of the magnetic unit cell.

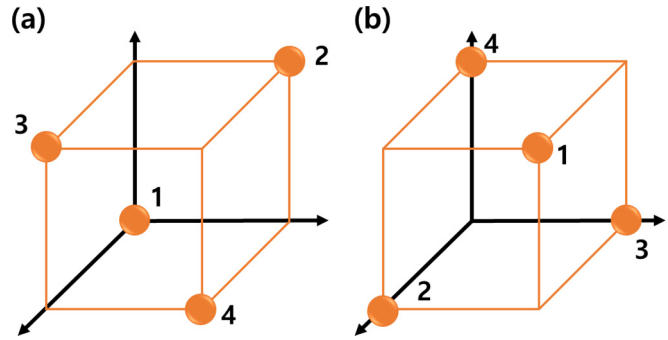


FIG. 16. Two clusters in pyrochlore iridates are shown. They are related by nonsymmorphic symmetry $\{P|T_{1/4,1/4,1/4}\}$.

### 2. CMMMs in pyrochlore iridates

If we consider the magnetic order of the wave vector $\vec{q} = 0$, a magnetic unit cell is just the same as a unit cell and an atomic cluster. We assume the length of the unit cell edge is 1.

There are two clusters, which are related by a nonsymmorphic symmetry operation $\{P|T_{1/4,1/4,1/4}\}$ (see Fig. 16). In a cluster, the number of degrees of freedom is twelve, since there are 3 moment directions and 4 atomic sites. Accordingly, we expect that dipoles, quadrupoles, and octupoles appear in the cluster, since the number of CMMM components is fifteen up to octupoles. We denote the $\alpha = x, y, z$ component of the magnetic moment of the $i$th site as $m_{i\alpha}$. Then, using Eq. (C4), the cluster dipoles are

$$\begin{aligned} M_{1\bar{1}} &= \frac{1}{\sqrt{2}}[m_{1x} + i m_{1y} + m_{2x} + i m_{2y} + m_{3x} + i m_{3y} + m_{4x} + i m_{4y}], \\ M_{10} &= m_{1z} + m_{2z} + m_{3z} + m_{4z}, \\ M_{11} &= \frac{1}{\sqrt{2}}[-m_{1x} + i m_{1y} - m_{2x} + i m_{2y} - m_{3x} + i m_{3y} - m_{4x} + i m_{4y}]. \end{aligned} \tag{C6}$$

The cluster quadrupoles for a cluster exist, but the total cluster quadrupoles are all zero, since the system is inversion-symmetric while quadrupoles are not [$M_{pq} = (-1)^{p+1} M_{pq}$]. Each cluster can have quadrupole moments; for example, cluster 1 [Fig. 16(a)] has

$$M^{(1)}_{2\bar{2}} = \frac{\sqrt{3}}{2}\left[e^{-i\frac{3\pi}{4}}(m_{1x} + i m_{1y}) + e^{i\frac{3\pi}{4}}(m_{2x} + i m_{2y}) + e^{-i\frac{\pi}{4}}(m_{3x} + i m_{3y}) + e^{i\frac{\pi}{4}}(m_{4x} + i m_{4y})\right],$$

$$M^{(1)}_{2\bar{1}} = \frac{\sqrt{3}}{2}\left[\frac{1}{\sqrt{2}}(-m_{1x} - i m_{1y} + m_{2x} + i m_{2y} + m_{3x} + i m_{3y} - m_{4x} - i m_{4y}) + e^{-i\frac{3\pi}{4}} m_{1z} + e^{i\frac{3\pi}{4}} m_{2z} + e^{-i\frac{\pi}{4}} m_{3z} + e^{i\frac{\pi}{4}} m_{4z}\right],$$

$$M^{(1)}_{20} = \frac{1}{2}[m_{1x} + m_{1y} - 2m_{1z} + m_{2x} - m_{2y} + 2m_{2z} - m_{3x} + m_{3y} + 2m_{3z} - m_{4x} - m_{4y} - 2m_{4z}],$$

$$M_{21}^{(1)} = \frac{\sqrt{3}}{2}\left[\frac{1}{\sqrt{2}}(m_{1x} - im_{1y} - m_{2x} + im_{2y} - m_{3x} + im_{3y} + m_{4x} - im_{4y}) + e^{-i\frac{\pi}{4}}m_{1z} + e^{i\frac{\pi}{4}}m_{2z} + e^{-i\frac{3\pi}{4}}m_{3z} + e^{i\frac{3\pi}{4}}m_{4z}\right],$$

$$M_{22}^{(1)} = \frac{\sqrt{3}}{2}\left[e^{i\frac{3\pi}{4}}(m_{1x} - im_{1y}) + e^{-i\frac{3\pi}{4}}(m_{2x} - im_{2y}) + e^{i\frac{\pi}{4}}(m_{3x} - im_{3y}) + e^{-i\frac{\pi}{4}}(m_{4x} - im_{4y})\right], \tag{C7}$$

and these are canceled out by the quadrupole moments of cluster 2. By the way, the cluster octupoles are

$$M_{3\bar{3}} = \frac{3\sqrt{5}}{8}i[m_{1x} + im_{1y} - m_{2x} - im_{2y} - m_{3x} - im_{3y} + m_{4x} + im_{4y}],$$

$$M_{3\bar{2}} = \frac{\sqrt{15}}{4}\left[e^{i\frac{\pi}{4}}(m_{1x} - m_{2y} + m_{3y} - m_{4x}) + e^{i\frac{3\pi}{4}}(m_{1y} + m_{2x} - m_{3x} - m_{4y}) + \frac{i}{\sqrt{2}}(m_{1z} - m_{2z} - m_{3z} + m_{4z})\right],$$

$$M_{3\bar{1}} = \frac{\sqrt{3}}{8}[-i(m_{1x} - m_{2x} - m_{3x} + m_{4x}) - (m_{1y} - m_{2y} - m_{3y} + m_{4y}) + 4\sqrt{2}\{e^{i\frac{\pi}{4}}(m_{1z} - m_{4z}) + e^{i\frac{3\pi}{4}}(m_{2z} - m_{3z})\}], \tag{C8}$$

$$M_{30} = \frac{3}{4}[-m_{1x} - m_{1y} + m_{2x} - m_{2y} - m_{3x} + m_{3y} + m_{4x} + m_{4y}],$$

$$M_{31} = \frac{\sqrt{3}}{8}\left[-i(m_{1x} - m_{2x} - m_{3x} + m_{4x}) + (m_{1y} - m_{2y} - m_{3y} + m_{4y}) + 4\sqrt{2}\left\{e^{i\frac{3\pi}{4}}(m_{1z} - m_{4z}) + e^{i\frac{\pi}{4}}(m_{2z} - m_{3z})\right\}\right],$$

$$M_{32} = \frac{\sqrt{15}}{4}\left[e^{-i\frac{\pi}{4}}(m_{1x} - m_{2y} + m_{3y} - m_{4x}) + e^{-i\frac{3\pi}{4}}(m_{1y} + m_{2x} - m_{3x} - m_{4y}) - \frac{i}{\sqrt{2}}(m_{1z} - m_{2z} - m_{3z} + m_{4z})\right],$$

$$M_{33} = \frac{3\sqrt{5}}{8}i[m_{1x} - im_{1y} - m_{2x} + im_{2y} - m_{3x} + im_{3y} + m_{4x} - im_{4y}].$$

### 3. Classification of CMMMs by irreducible representations

Multipole moments can be classified by irreducible representations (irreps) of the symmetry group [27,28,40–43]. We can classify CMMMs in the same way.

Applying projection operators for CMMMs [44], we classify CMMMs by irreps. Symmetrized CMMMs can be considered as order parameters, since symmetrized CMMMs represent the degree of symmetry breaking. In Table I and Fig. 17, we show symmetrized CMMMs as the linear combination of CMMMs and as a configuration of the magnetic moments in the lattice.

In order to analyze the symmetry properties of $J = 3/2$ states at the quadratic band crossing, let us concentrate only

TABLE I. CMMMs are classified into the irreps of the $T_d$ group. The table is very similar to CMMMs in Ref. [27]. We show two kinds of group representations in the second column: $T_1$, $E$, $A_2$, $T_2$ are for the $T_d$ single group, and $\Gamma_i$ are for the double group.

| Multipole | Irrep | CMMM |
|---|---|---|
| Dipole | $T_1$ ($\Gamma_4$) | $N_x \equiv \frac{M_{1\bar{1}} - M_{11}}{\sqrt{2}}$ |
| | | $N_y \equiv \frac{M_{1\bar{1}} + M_{11}}{\sqrt{2}i}$ |
| | | $N_z \equiv M_{10}$ |
| Quadrupole | $E$ ($\Gamma_3$) | $Q_{3z^2-r^2} \equiv M_{20}$ |
| | | $Q_{x^2-y^2} \equiv \frac{1}{\sqrt{2}}(M_{22} + M_{2\bar{2}})$ |
| | $T_1$ ($\Gamma_4$) | $Q_{yz} \equiv -\frac{i}{\sqrt{2}}(M_{21} + M_{2\bar{1}})$ |
| | | $Q_{zx} \equiv \frac{1}{\sqrt{2}}(-M_{21} + M_{2\bar{1}})$ |
| | | $Q_{xy} \equiv \frac{i}{\sqrt{2}}(M_{22} - M_{2\bar{2}})$ |
| Octupole | $A_2$ ($\Gamma_2$) | $T_{xyz} \equiv \frac{i}{\sqrt{2}}(M_{32} - M_{3\bar{2}})$ |
| | $T_1$ ($\Gamma_4$) | $T_x^1 \equiv \frac{1}{4}[\sqrt{5}(-M_{33} + M_{3\bar{3}}) - \sqrt{3}(-M_{31} + M_{3\bar{1}})]$ |
| | | $T_y^1 \equiv \frac{i}{4}[\sqrt{5}(M_{33} + M_{3\bar{3}}) + \sqrt{3}(M_{31} + M_{3\bar{1}})]$ |
| | | $T_z^1 \equiv M_{30}$ |
| | $T_2$ ($\Gamma_5$) | $T_x^2 \equiv \frac{1}{4}[\sqrt{5}(M_{31} - M_{3\bar{1}}) + \sqrt{3}(M_{33} - M_{3\bar{3}})]$ |
| | | $T_y^2 \equiv \frac{-i}{4}[\sqrt{5}(M_{31} + M_{3\bar{1}}) - \sqrt{3}(M_{33} + M_{3\bar{3}})]$ |
| | | $T_z^2 \equiv \frac{1}{\sqrt{2}}(M_{32} + M_{3\bar{2}})$ |

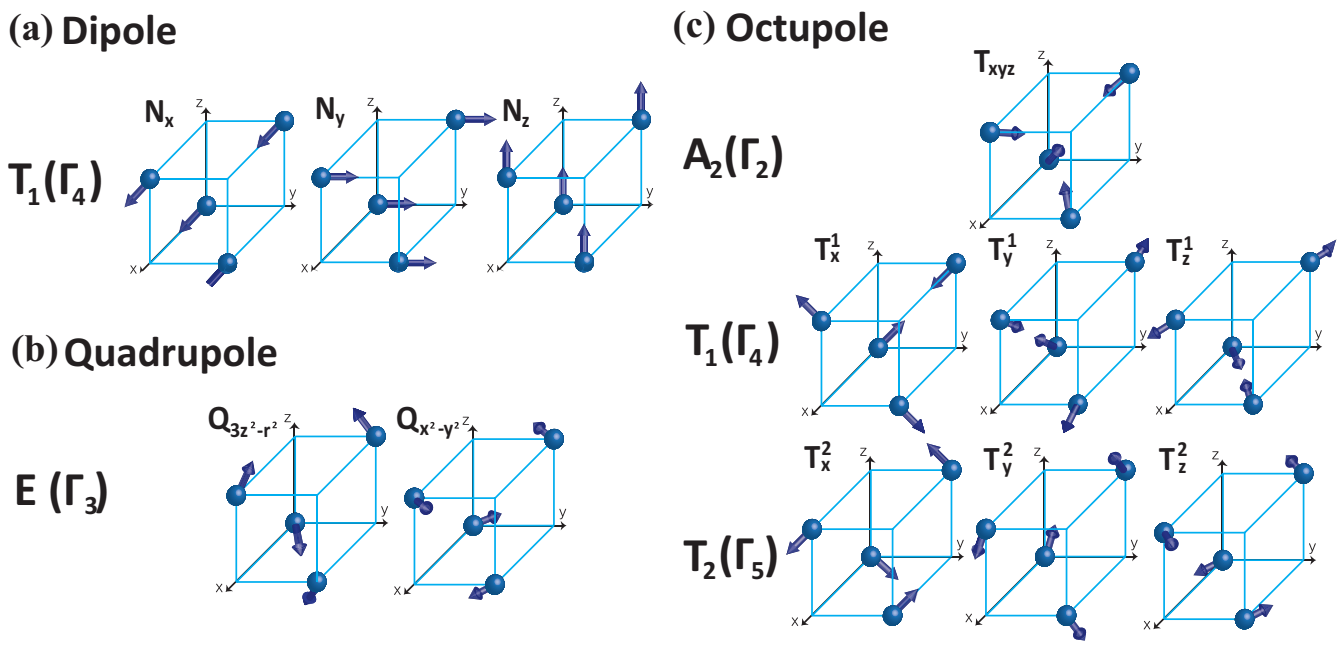


FIG. 17. Each symmetrized CMMM in Table I is depicted in the first cluster of pyrochlore iridates with its group representation. The configurations of $T_x^1, T_y^1, T_z^1$ are just the same as those of $Q_{yz}, Q_{zx}, Q_{xy}$. Due to the inversion symmetry, the quadrupole will be canceled by the second cluster.

on cluster 1. Since there are 12 degrees of freedom in cluster 1, we have 12 independent symmetrized CMMMs. However, up to the octupole, there should be 15 $(3+5+7)$ order parameters. In fact, 3 octupolar symmetrized CMMMs $T_x^1, T_y^1, T_z^1$ correspond to the symmetrized quadrupoles $Q_{yz}, Q_{zx}, Q_{xy}$. Thus, the number of independent CMMMs is just the same as the number of degrees of freedom.

However, in the presence of inversion symmetry, the quadrupole must vanish due to its oddness under inversion; then only dipoles and octupoles can exist in pyrochlore iridates. We clearly prove the statement by adding the configuration of cluster 2 to that of cluster 1. For cluster 2, the orientation of magnetic moment at each site is opposite to that in cluster 1 only in the quadrupole order.

## APPENDIX D: THE LATTICE MODEL

### 1. Phase diagrams

The tight-binding model Hamiltonian is $H_{TB} = H_0 + H_U + H_Z$ [8]. First,

$$H_0 = \sum_{\langle ij\rangle} c_i^\dagger (t_1 + it_2 \mathbf{d_{ij}} \cdot \vec{\sigma}) c_j + \sum_{\langle\langle ij\rangle\rangle} c_i^\dagger (t_1' + i[t_2' \mathbf{R_{ij}} + t_3' \mathbf{D_{ij}}] \cdot \vec{\sigma}) c_j, \tag{D1}$$

where it describes the nearest- and next-nearest-neighbor hopping. Note that the hopping vectors are defined as

$$\begin{aligned} &\mathbf{d}_{ij} = 2\mathbf{A}_{ij} \times \mathbf{B}_{ij}, \quad \mathbf{A}_{ij} = \tfrac{1}{2}(\mathbf{b}_i + \mathbf{b}_j) - \mathbf{c}, \\ &\mathbf{B}_{ij} = \mathbf{b}_j - \mathbf{b}_i, \quad \mathbf{R}_{ij} = \mathbf{B}_{ik} \times \mathbf{B}_{kj}, \\ &\mathbf{D}_{ij} = \mathbf{d}_{ik} \times \mathbf{d}_{kj}, \end{aligned} \tag{D2}$$

where $\mathbf{b}_i$ is the position of the $i$th atom in the unit cell, and $\mathbf{c}$ is the position of the center of the unit cell. The hopping parameters are defined as

$$\begin{aligned} t_1 &= \tfrac{130}{243} t_{\mathrm{oxy}} + \tfrac{17}{324} t_\sigma - \tfrac{79}{243} t_\pi, \\ t_2 &= \tfrac{28}{243} t_{\mathrm{oxy}} + \tfrac{15}{243} t_\sigma - \tfrac{40}{243} t_\pi, \\ t_1' &= \tfrac{233}{2916} t_\sigma' - \tfrac{407}{2187} t_\pi', \\ t_2' &= \tfrac{1}{1458} t_\sigma' + \tfrac{220}{2187} t_\pi', \\ t_3' &= \tfrac{17}{324} t_\sigma' + \tfrac{460}{2187} t_\pi', \end{aligned}$$

where $t'_{\sigma,\pi} = \alpha t_{\sigma,\pi}$.

Second, the Hubbard repulsion Hamiltonian $H_U$ is

$$H_U = U \sum_{Ri} n_{Ri\uparrow} n_{Ri\downarrow}, \tag{D3}$$

where $n_{Ris}$ is the number operator of iridium electrons whose effective angular momentum is 1/2. We apply the Hartree-Fock approximation to this Hubbard repulsion term:

$$\begin{aligned} H_U^{MF} &= -U \left( \sum_{Ri} 2\langle \vec{m}_{R,i} \rangle \cdot \vec{m}_{R,i} - \langle \vec{m}_{R,i} \rangle^2 \right), \\ \vec{m}_{R,i} &= \frac{1}{2N} \sum_{\alpha,\beta=\uparrow,\downarrow} c_{Ri\alpha}^\dagger \sigma_{\alpha,\beta} c_{Ri\beta}, \end{aligned} \tag{D4}$$

where $N$ is the total number of unit cells in the lattice.

Finally, we have Zeeman coupling for Ir electrons, whose effective angular momentum is 1/2:

$$H_Z = -\frac{1}{2} \sum_{Ris} c_{Ris}^\dagger (\vec{H} \cdot \vec{\sigma}_{ss'}) c_{Ris'}. \tag{D5}$$

We can add an additional interaction into this Hamiltonian, which couples rare-earth $f$ electrons to iridium $d$ electrons [20]. Since $f$ electrons also have spins, we should consider the Zeeman effect for $f$ electrons. The Hamiltonian is $H' = H + H_{fd} + H'_z$, where

$$H_{fd} = J_{fd} \sum_{\langle iJ \rangle} \sum_{\mu,\nu=x,y,z} \Lambda_{iJ}^{\mu\nu} \sigma_i^\mu \tau_J^\nu,$$
$$H'_z = -\sum_I \gamma (\vec{H} \cdot \vec{a}_I) \tau_I^z. \tag{D6}$$

Here, $J_{fd}$ is the coupling constant, $\tau_I^\mu$ are the rare-earth $f$-electron spins which are Ising-like along the local [111] direction, $\gamma$ is the $f$-electron $g$ factor, and $\Lambda_{iJ}^{\mu\nu}$ are defined [20] as

$$\Lambda_{iJ}^{\mu\nu} = \begin{bmatrix} [G_1^x \vec{a}_J + G_2^x \vec{a}_J \bar{\times} (\vec{d}_{iJ} \bar{\times} \vec{d}_{iJ})] \cdot \hat{e}_\mu, & (\nu = x) \\ G^y \vec{a}_J \times (\vec{d}_{iJ} \bar{\times} \vec{d}_{iJ}) \cdot \hat{e}_\mu, & (\nu = y) \\ [G_1^z \vec{a}_J + G_2^z \vec{a}_J \bar{\times} (\vec{d}_{iJ} \bar{\times} \vec{d}_{iJ})] \cdot \hat{e}_\mu, & (\nu = z) \end{bmatrix},$$

for $Nd^{3+}$, which is a Kramers ion. Here, $i$, $j$ are for the iridium site while $I$, $J$ are for the rare-earth site. However, for $Pr^{3+}$, which is a non-Kramers ion,

$$\Lambda_{iJ}^{\mu\nu} = \begin{bmatrix} 0, & (\nu = x) \\ 0, & (\nu = y) \\ [G_1^z \vec{a}_J + G_2^z \vec{a}_J \bar{\times} (\vec{d}_{iJ} \bar{\times} \vec{d}_{iJ})] \cdot \hat{e}_\mu, & (\nu = z) \end{bmatrix}.$$

Furthermore, Pr in-plane components can couple to the charge density of Ir electrons [31].

We obtain the ground state energy band and magnetic moment configuration through self-consistent mean-field theory under various Hubbard strengths $U$ and magnetic field strengths $H$ for $Nd_2Ir_2O_7$. Then, we investigate crossing points within the Brillouin zone to determine topological phases, and exhibit the general phase diagrams with different parameters in Figs. 7 and 18.

### 2. Projection of the effective Zeeman field onto the effective theory

We can consider Hubbard repulsion, $fd$ exchange, and the magnetic field together in the effective field which is applied for each iridium spin. Then the interaction Hamiltonian is just an effective Zeeman term,

$$H_B = H_U^{MF} + H_{fd} + H_Z$$
$$= \frac{1}{2} \sum_i \vec{B}_{\text{eff},i} \cdot [c_{i,s}^\dagger \vec{\sigma}_{ss'} c_{i,s'}] + \text{const.}, \tag{D7}$$

where

$$\frac{1}{2} B_{\text{eff},i}^\mu = -\frac{U}{2} \langle \sigma_i^\mu \rangle + J_{fd} \sum_{J,\nu} \Lambda_{iJ}^{\mu\nu} \tau_J^\nu - \frac{1}{2} H^\mu. \tag{D8}$$

Since the magnetic moment has the same symmetric properties as the effective field, we can define symmetrized CMMMs in terms of the effective field instead of magnetic moments. That is, the magnetic moments in Eqs. (C6), (C7), (C8) are just replaced with $\vec{B}_{\text{eff},i}$. After then, let us define some order parameters with effective field based symmetrized CMMMs. The AIAO order parameter is defined as

$$M_{A_2} = \frac{1}{8} \sum_i \vec{B}_{\text{eff},i} \cdot \vec{a}_i = \frac{1}{2\sqrt{15}} T_{xyz}, \tag{D9}$$

such that $\vec{a}_i$ is the unit vector directing from the $i$th site to the center of the tetrahedron. This changes as the $\Gamma_2$ representation of the $T_d$ double group. The magnetization is defined as

$$M_{D,\mu} = \frac{1}{8} \sum_i B_{\text{eff},i\mu} = \frac{1}{8} N_\mu, \tag{D10}$$

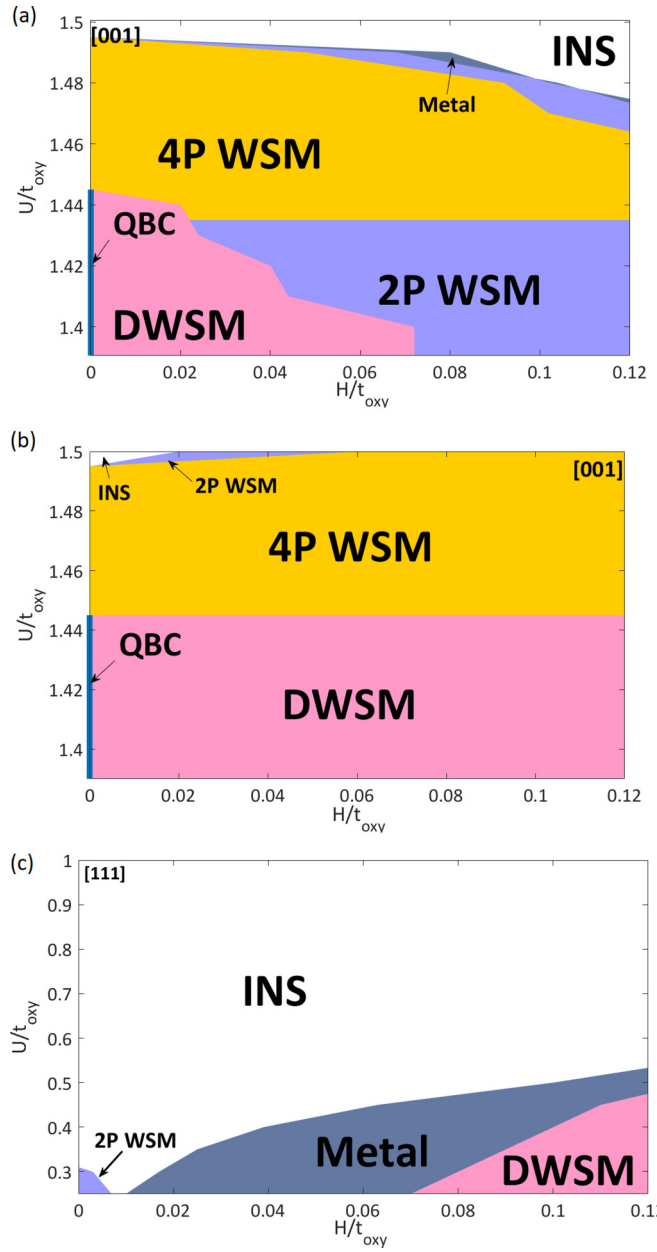


FIG. 18. General phase diagrams from self-consistent mean-field theory. (a) $t_\sigma = -0.8, \alpha = 0.08, J_{fd} = 0,$ [001] field. Heisenberg Ir spin. (b) $t_\sigma = -0.8, \alpha = 0.08, J_{fd} = 0,$ [001] field. Ising Ir spin. (c) $t_\sigma = -1.1, \alpha = 0.02, J_{fd} = 1,$ [111] field. Heisenberg Ir spin.

where $\mu = x, y, z$. The 2I2O order parameter is defined by the $T_1$ octupole $(T_x^1, T_y^1, T_z^1)$,

$$\begin{aligned} M_{T_1,x} &= \tfrac{1}{12}(B_{\mathrm{eff},1y} + B_{\mathrm{eff},1z} - B_{\mathrm{eff},2y} - B_{\mathrm{eff},2z} - B_{\mathrm{eff},3y} \\ &\quad + B_{\mathrm{eff},3z} + B_{\mathrm{eff},4y} - B_{\mathrm{eff},4z}) = -\tfrac{1}{9}T_x^1, \\ M_{T_1,y} &= \tfrac{1}{12}(B_{\mathrm{eff},1x} + B_{\mathrm{eff},1z} - B_{\mathrm{eff},2x} + B_{\mathrm{eff},2z} - B_{\mathrm{eff},3x} \\ &\quad - B_{\mathrm{eff},3z} + B_{\mathrm{eff},4x} - B_{\mathrm{eff},4z}) = -\tfrac{1}{9}T_y^1, \\ M_{T_1,z} &= \tfrac{1}{12}(B_{\mathrm{eff},1x} + B_{\mathrm{eff},1y} - B_{\mathrm{eff},2x} + B_{\mathrm{eff},2y} + B_{\mathrm{eff},3x} \\ &\quad - B_{\mathrm{eff},3y} - B_{\mathrm{eff},4x} - B_{\mathrm{eff},4y}) = -\tfrac{1}{9}T_z^1. \end{aligned} \tag{D11}$$

Those order parameters commonly appear for both the [001] and [111] direction fields.

For the projection of the lattice model, we find $J_z$ eigenstates from taking fourfold degenerate eigenstates of $H_0$ at the $\Gamma$ point [Fig. 6(a)]. $J_z$ eigenstates $\{|\psi_{j_z}\rangle\}$ are

$$\begin{aligned} |\psi_{3/2}\rangle &= \frac{1}{2}\left(e^{i\frac{3\pi}{4}}, e^{i\frac{\pi}{4}}, e^{-i\frac{3\pi}{4}}, e^{-i\frac{\pi}{4}}, 0, 0, 0, 0\right)^T, \\ |\psi_{1/2}\rangle &= \frac{1}{\sqrt{6}}\left(-i, i, i, -i, \frac{-1+i}{2}, \frac{1+i}{2}, \frac{-1-i}{2}, \frac{1-i}{2}\right)^T, \\ |\psi_{-1/2}\rangle &= \frac{1}{\sqrt{6}}\left(\frac{-1-i}{2}, \frac{1-i}{2}, \frac{-1+i}{2}, \frac{1+i}{2}, -i, i, i, -i\right)^T, \\ |\psi_{-3/2}\rangle &= \frac{1}{2}\left(0, 0, 0, 0, e^{-i\frac{3\pi}{4}}, e^{-i\frac{\pi}{4}}, e^{i\frac{3\pi}{4}}, e^{i\frac{\pi}{4}}\right)^T. \end{aligned} \tag{D12}$$

Then, the projection matrix is just $P = \sum_{j_z} |\psi_{j_z}\rangle\langle\psi_{j_z}|$.

We have total 12 degrees of freedom (4 sites $\times$ 3 directions), but we can reduce the number of parameters to 4 by symmetry. Considering $C_{2z}$ and $\sigma_d T$, the symmetries under the [001] magnetic field and AIAO order, we have in general

$$\begin{aligned} \vec{B}_{\mathrm{eff},1} &= (B_{\mathrm{eff},1x}, B_{\mathrm{eff},1x}, B_{\mathrm{eff},1z}), \\ \vec{B}_{\mathrm{eff},2} &= (B_{\mathrm{eff},2x}, -B_{\mathrm{eff},2x}, B_{\mathrm{eff},2z}), \\ \vec{B}_{\mathrm{eff},3} &= (-B_{\mathrm{eff},2x}, B_{\mathrm{eff},2x}, B_{\mathrm{eff},2z}), \\ \vec{B}_{\mathrm{eff},4} &= (-B_{\mathrm{eff},1x}, -B_{\mathrm{eff},1x}, B_{\mathrm{eff},1z}). \end{aligned} \tag{D13}$$

Under the magnetic moment configuration, the order parameters are

$$\begin{aligned} M_{A_2} &= \frac{1}{8\sqrt{3}}(4B_{\mathrm{eff},1x} + 2B_{\mathrm{eff},1z} + 4B_{\mathrm{eff},2x} - 2B_{\mathrm{eff},2z}), \\ M_{D,z} &= \frac{1}{4}(B_{\mathrm{eff},1z} + B_{\mathrm{eff},2z}), \\ M_{T_1,z} &= \frac{1}{3}(B_{\mathrm{eff},1x} - B_{\mathrm{eff},2x}). \end{aligned} \tag{D14}$$

We can now express the projection of the effective Zeeman term as

$$P^\dagger H_B P = \left[M_{A_2}\Gamma_{45} + \left(\tfrac{2}{3}M_{D,z} - \tfrac{9}{4}M_{T_1,z}\right)J_z - M_{T_1,z}J_z^3\right]. \tag{D15}$$

On the other hand, if we consider $C_{3,[111]}$ and $\sigma_{d,[111]}T$, the symmetries under the [111] magnetic field and AIAO order, we can reduce the number of parameters to 3 by symmetry:

$$\begin{aligned} \vec{B}_{\mathrm{eff},1} &= (B_{\mathrm{eff},1x}, B_{\mathrm{eff},1x}, B_{\mathrm{eff},1x}), \\ \vec{B}_{\mathrm{eff},2} &= (B_{\mathrm{eff},2x}, B_{\mathrm{eff},2y}, B_{\mathrm{eff},2y}), \\ \vec{B}_{\mathrm{eff},3} &= (B_{\mathrm{eff},2y}, B_{\mathrm{eff},2x}, B_{\mathrm{eff},2y}), \\ \vec{B}_{\mathrm{eff},4} &= (B_{\mathrm{eff},2y}, B_{\mathrm{eff},2y}, B_{\mathrm{eff},2x}). \end{aligned} \tag{D16}$$

In this configuration, the order parameters are

$$\begin{aligned} M_{A_2} &= \frac{\sqrt{3}}{8}(B_{\mathrm{eff},1x} + B_{\mathrm{eff},2x} - 2B_{\mathrm{eff},2y}), \\ M_{D,x} &= M_{D,y} = M_{D,z} = \frac{1}{8}(B_{\mathrm{eff},1x} + B_{\mathrm{eff},2x} + 2B_{\mathrm{eff},2y}), \\ M_{T_1,x} &= M_{T_1,y} = M_{T_1,z} = \frac{1}{6}(B_{\mathrm{eff},1x} - B_{\mathrm{eff},2x}). \end{aligned} \tag{D17}$$

The projection of the effective Zeeman term under the [111] field is

$$P^\dagger H_B P = \left[M_{A_2}\Gamma_{45} + \left(\tfrac{2}{3}\vec{M}_D - \tfrac{9}{4}\vec{M}_{T_1}\right)\cdot\vec{J} - \vec{M}_{T_1}\cdot\vec{J}^3\right]. \tag{D18}$$

For both cases, we obtain $\theta$ and $\phi$,

$$\begin{aligned} \theta &= \arctan\frac{M_{T_1,z}}{\frac{2}{3}M_{D,z} - \frac{9}{4}M_{T_1,z}}, \\ \phi &= \arctan\frac{\frac{2}{3}M_{D,z} - \frac{9}{4}M_{T_1,z}}{M_{A_2}\cos\theta}. \end{aligned} \tag{D19}$$


[1] W. Witczak-Krempa, G. Chen, Y. B. Kim, and L. Balents, Annu. Rev. Condens. Matter Phys. **5**, 57 (2014).

[2] R. Schaffer, E. K.-H. Lee, B.-J. Yang, and Y. B. Kim, Rep. Prog. Phys. **79**, 094504 (2016).

[3] X. Wan, A. M. Turner, A. Vishwanath, and S. Y. Savrasov, Phys. Rev. B **83**, 205101 (2011).

[4] B. Lv, H. Weng, B. Fu, X. Wang, H. Miao, J. Ma, P. Richard, X. Huang, L. Zhao, G. Chen *et al.*, Phys. Rev. X **5**, 031013 (2015).

[5] H. Weng, C. Fang, Z. Fang, B. A. Bernevig, and X. Dai, Phys. Rev. X **5**, 011029 (2015).

[6] S.-M. Huang, S.-Y. Xu, I. Belopolski, C.-C. Lee, G. Chang, B. Wang, N. Alidoust, G. Bian, M. Neupane, C. Zhang *et al.*, Nat. Commun. **6**, 7373 (2015).

[7] S.-Y. Xu, I. Belopolski, N. Alidoust, M. Neupane, G. Bian, C. Zhang, R. Sankar, G. Chang, Z. Yuan, C.-C. Lee *et al.*, Science **349**, 613 (2015).

[8] W. Witczak-Krempa, A. Go, and Y. B. Kim, Phys. Rev. B **87**, 155101 (2013).

[9] T. Kondo, M. Nakayama, R. Chen, J. Ishikawa, E.-G. Moon, T. Yamamoto, Y. Ota, W. Malaeb, H. Kanai, Y. Nakashima *et al.*, Nat. Commun. **6**, 10042 (2015).

[10] M. Kurita, Y. Yamaji, and M. Imada, J. Phys. Soc. Jpn. **80**, 044708 (2011).
[11] K. Tomiyasu, K. Matsuhira, K. Iwasa, M. Watahiki, S. Takagi, M. Wakeshima, Y. Hinatsu, M. Yokoyama, K. Ohoyama, and K. Yamada, J. Phys. Soc. Jpn. **81**, 034709 (2012).
[12] W. Witczak-Krempa and Y. B. Kim, Phys. Rev. B **85**, 045124 (2012).
[13] K. Ueda, T. Oh, B.-J. Yang, R. Kaneko, J. Fujioka, N. Nagaosa, and Y. Tokura, Nat. Commun. **8**, 15515 (2017).
[14] Y. Machida, S. Nakatsuji, Y. Maeno, T. Tayama, T. Sakakibara, and S. Onoda, Phys. Rev. Lett. **98**, 057203 (2007).
[15] L. Balicas, S. Nakatsuji, Y. Machida, and S. Onoda, Phys. Rev. Lett. **106**, 217204 (2011).
[16] S. M. Disseler, S. R. Giblin, C. Dhital, K. C. Lukas, S. D. Wilson, and M. J. Graf, Phys. Rev. B **87**, 060403 (2013).
[17] K. Ueda, J. Fujioka, Y. Takahashi, T. Suzuki, S. Ishiwata, Y. Taguchi, M. Kawasaki, and Y. Tokura, Phys. Rev. B **89**, 075127 (2014).
[18] K. Ueda, J. Fujioka, B.-J. Yang, J. Shiogai, A. Tsukazaki, S. Nakamura, S. Awaji, N. Nagaosa, and Y. Tokura, Phys. Rev. Lett. **115**, 056402 (2015).
[19] E. Y. Ma, Y.-T. Cui, K. Ueda, S. Tang, K. Chen, N. Tamura, P. M. Wu, J. Fujioka, Y. Tokura, and Z.-X. Shen, Science **350**, 538 (2015).
[20] Z. Tian, Y. Kohama, T. Tomita, H. Ishizuka, T. H. Hsieh, J. J. Ishikawa, K. Kindo, L. Balents, and S. Nakatsuji, Nat. Phys. **12**, 134 (2016).
[21] P. Goswami, B. Roy, and S. Das Sarma, Phys. Rev. B **95**, 085120 (2017).
[22] G. Chen and M. Hermele, Phys. Rev. B **86**, 235129 (2012).
[23] J. Cano, B. Bradlyn, Z. Wang, M. Hirschberger, N. P. Ong, and B. A. Bernevig, Phys. Rev. B **95**, 161306 (2017).
[24] J. Luttinger, Phys. Rev. **102**, 1030 (1956).
[25] J. Hensel and K. Suzuki, Phys. Rev. Lett. **22**, 838 (1969).
[26] A. V. Nenashev, A. V. Dvurechenskii, and A. F. Zinovieva, Phys. Rev. B **67**, 205301 (2003).
[27] M.-T. Suzuki, T. Koretsune, M. Ochi, and R. Arita, Phys. Rev. B **95**, 094406 (2017).
[28] H. Kusunose, J. Phys. Soc. Jpn. **77**, 064710 (2008).
[29] S. B. Lee, S. Onoda, and L. Balents, Phys. Rev. B **86**, 104412 (2012).
[30] Y.-P. Huang, G. Chen, and M. Hermele, Phys. Rev. Lett. **112**, 167203 (2014).
[31] S. B. Lee, A. Paramekanti, and Y. B. Kim, Phys. Rev. Lett. **111**, 196601 (2013).
[32] S. Murakami, N. Nagaosa, and S.-C. Zhang, Phys. Rev. Lett. **93**, 156804 (2004).
[33] E.-G. Moon, C. Xu, Y. B. Kim, and L. Balents, Phys. Rev. Lett. **111**, 206401 (2013).
[34] L. Savary, E.-G. Moon, and L. Balents, Phys. Rev. X **4**, 041027 (2014).
[35] H. Isobe and N. Nagaosa, Phys. Rev. B **86**, 165127 (2012).
[36] H. Isobe and N. Nagaosa, Phys. Rev. B **87**, 205138 (2013).
[37] B.-J. Yang, E.-G. Moon, H. Isobe, and N. Nagaosa, Nat. Phys. **10**, 774 (2014).
[38] P. Goswami and S. Chakravarty, Phys. Rev. Lett. **107**, 196803 (2011).
[39] Y. Wang and R. M. Nandkishore, Phys. Rev. B **96**, 115130 (2017).
[40] T. Takimoto, J. Phys. Soc. Jpn. **75**, 034714 (2006).
[41] A. Kiss and P. Fazekas, Phys. Rev. B **71**, 054415 (2005).
[42] R. Shiina, H. Shiba, and P. Thalmeier, J. Phys. Soc. Jpn. **66**, 1741 (1997).
[43] P. Santini, S. Carretta, G. Amoretti, R. Caciuffo, N. Magnani, and G. H. Lander, Rev. Mod. Phys. **81**, 807 (2009).
[44] M. S. Dresselhaus, G. Dresselhaus, and A. Jorio, *Group Theory: Application to the Physics of Condensed Matter* (Springer Science & Business Media, 2007).